RNA Pol I activity maintains chromatin condensation and the H3K4me3 gradient essential for oogenesis, independent of ribosome production

Raquel Mejia-Trujillo[1], Qiuxia Zhao[1], Ayesha Rahman[1], Elif Sarinay Cenik[1,†]

[1] Department of Molecular Biosciences, University of Texas at Austin, Austin, TX 78712, USA
[†] Corresponding author: esarinay@utexas.edu

ABSTRACT

Oogenesis requires extensive and dynamic chromatin remodeling that primes gene promoters for later transcriptional activation during embryonic development. Here, we uncover a pivotal, non-canonical role for RNA Polymerase I (Pol I) in driving these chromatin state transitions during *Caenorhabditis elegans* oogenesis. Using the auxin-inducible degron system to selectively deplete either a Pol I-specific catalytic subunit or a ribosome assembly factor, we disentangle the consequences of impaired nucleolar integrity from reductions in ribosome biogenesis. Strikingly, although disrupting ribosome assembly caused minimal effects on oocyte production, loss of nucleolar structure via Pol I depletion led to severe meiotic chromosome abnormalities, widespread changes in chromatin accessibility, and a dampening of the typical distal-proximal H3K4me3 gradient required for oogenesis, resulting in fewer but significantly larger oocytes. Despite their promoters becoming more accessible, oogenesis genes did not show large changes in steady-state mRNA, consistent with transcriptional repression prior to fertilization. Instead, Pol I depletion prematurely remodeled oogenic chromatin, through a misdirection of H3K4me3 deposition towards promoters normally primed for zygotic genome activation. These findings reveal an epigenetic gating function for nucleolar integrity in oocyte maturation: Pol I preserves three-dimensional chromatin organization and maintains proper spatiotemporal regulation of histone modifications, independent of ribosome production. Given the evolutionary conservation of nucleolar dynamics and histone modifications during gametogenesis, our work suggests that nucleolar stress, whether from environmental factors, aging, or genetic disorders, could broadly compromise fertility by disrupting oogenic chromatin priming.

INTRODUCTION

Chromosome condensation and chromatin modifications during meiosis are essential to ensure accurate genetic transmission in sexually reproducing species. In the hermaphroditic germline of *Caenorhabditis elegans*, female gamete production proceeds through four distinct zones: mitotic proliferation, transition, meiosis I, and oocyte maturation. Upon completion of oocyte maturation, the most proximal oocyte is fertilized by the adjacent spermatheca, initiating zygotic development.

Oogenesis involves a complex progression of germ cell maturation, yet net transcriptional activity is strikingly low in late stage oocytes. Instead, many oogenesis genes remain largely quiescent before fertilization, with regulation relying primarily on extensive chromatin remodeling. This epigenetic priming prepares the promoters of key developmental genes to be robustly activated after fertilization or during early embryogenesis [1–3].

In *C. elegans*, as in other species, germ cells undergo profound chromatin reorganization during meiotic progression to form specialized meiotic chromatin structures, establish parental imprinting marks, and position active marks near the promoters of genes that will be engaged during zygotic genome activation (ZGA) [4]. Specifically, H3K4me3 marks shift from gene bodies to promoters as undifferentiated mitotic germ cells progress through meiosis I [4]. This promoter-specific priming of ZGA genes with H3K4me3 is evolutionarily conserved across species, including *Xenopus* [5], zebrafish [6,7], mice [8,9], and humans [10] and is critical for normal germline development. For instance, *C. elegans* germlines lacking H3K4 methyltransferase activity exhibit reduced oocyte production, aberrant nuclear morphology, and aneuploid gametes [11,12], while deficient H3K4 demethylase activity leads to abnormal chromatin condensation, diminished oocyte production, and failed entry into meiosis [13].

In parallel with the spatiotemporal regulation of H3K4 methylation, maturing germ cells also temporally regulate nucleolar activity during oogenesis. The nucleolus [14], responsible for rRNA synthesis and ribosome assembly, remains intact throughout meiosis but temporarily disassembles at the onset of oocyte maturation before reappearing during ZGA [15]. Similar nucleolar dynamics have been documented across hermaphrodite and dioecious eukaryotes, including *C. elegans*, yeast, pig, and mouse [15–20]. The presence of the nucleolus throughout oogenesis is unsurprising [21], given that maternal ribosome production is sufficient to drive embryogenesis in *Caenorhabditis elegans* [22]; however, the nucleolus may have additional roles beyond ribosome production during oogenesis. For example, in *Arabidopsis*, rDNA loci are embedded within the nucleolus to prevent alterations of rDNA copy numbers and genomic instability during meiotic homologous recombination [23]. In mouse oocytes, maternal nucleolar components are essential for maintaining satellite repeat sequences immediately after fertilization [24]. Lastly, the nucleolar microenvironment in *C. elegans* can sequester transcriptional silencing factors, such as PIE-1, away from the genome to promote transcription during late oogenesis [25].

Despite these hints of broader functions for the nucleolus, dissecting its direct contributions to oogenesis has been challenging because rRNA synthesis, ribosome assembly, and the maintenance of a spatially distinct nuclear subcompartment are all interconnected. For example, RNA Polymerase I (Pol I) transcription of rDNA loci is accompanied by co-transcriptional processing of pre-rRNA, followed by co-assembly with ribosomal proteins into ribosome subunits [26]. The nucleolar microenvironment is similarly co-dependent on these other functions, as its liquid-liquid phase-separated properties make its spherical

morphology reliant on active rDNA transcription and subsequent processing and assembly [27,28]. Thus, similar to how separation-of-function mutations in proteins are used to differentiate between distinct protein functions [29–31], there is a demand for genetic tools that can isolate interconnected functions of the same subcellular structure. Here, we utilized two separation-of-function *C. elegans* strains to identify potential nucleolar functions that are independent from ribosome production during oogenesis.

Using the auxin-inducible degron (AID) system, we targeted either a catalytic subunit specific to RNA Pol I (orthologous to human *POL1RB*) or a ribosome assembly factor (orthologous to human *GRWD1*). This approach isolates the impact of nucleolar disruption on female germ cell maturation from perturbed downstream ribosome assembly. Our results uncover a non-ribosomal function of RNA Pol I in regulating oocyte production, meiotic chromosome morphology and chromatin landscape, and the maintenance of an essential H3K4 methylation gradient. Germ cells fail to regulate chromatin remodeling during the transition from mitotic proliferation to meiotic prophase I following reduced RNA Pol I activity, but not after a decrease in ribosome assembly. ATAC-seq analyses further reveal that chromatin accessibility increases near oogenesis promoters, oogenesis-promoting EFL-1-binding sites, and promoters subject to canonical H3K4me3 remodeling during oogenesis. Nucleolar disruption also dampened the distal-proximal H3K4me3 gradient through premature H3K4me3 deposition. Collectively, our data suggests that nucleolar integrity, maintained by RNA Pol I activity, is involved in the coordination of chromatin remodeling during oogenesis, ensuring the production of healthy, properly sized oocytes.

RESULTS

Persistence and dynamics of nucleolar structure during *Caenorhabditis elegans* germline development and oogenesis

We first examined nucleolar morphology in a wild-type background to establish a baseline representation of its structure during germline development, from the mitotic through meiotic zones, and into oocyte maturation. To accomplish this, we fluorescently tagged two proteins: NUCL-1, the *Caenorhabditis elegans* ortholog of human Nucleolin, which facilitates rRNA transcription and processing [32–34], and DAO-5, the ortholog of human Nopp140, required for nucleologenesis and rDNA transcription [15,35]. We also used a labeled SYP-3, a key component of the synaptonemal complex [36,37], to distinguish between different germline zones. Cells distal to synaptonemal complex formation were classified as mitotic, cells displaying a synaptonemal complex were assigned to the transition or pachytene zone, and cells with visible plasma membrane under transmitted photomultiplier tubes (T-PMT) were defined as being in the oocyte maturation zone.

A three-dimensional confocal projection of an adult gonad arm demonstrated that NUCL-1 retains a spherical nucleolar localization pattern in the mitotic, meiotic, and most of the oocyte maturation zone, as indicated by distinct SYP-3 localization (**Figure 1A**). As the oocytes matured, NUCL-1 and DAO-5 formed intermediate droplet-like structures in the "-2" oocyte (the second-most proximal oocyte), followed by a complete dissolution of nucleolus in the "-1" oocyte (the most proximal one) (**Figure 1B** and **1C**). These results suggest that nucleolar integrity is largely maintained from the distal mitotic region through meiosis, but is disrupted just before fertilization. This observation agrees with previous reports in *C. elegans* germlines [15,38,39] and is also conserved in mammalian oocytes [16,18–20].

Figure 1

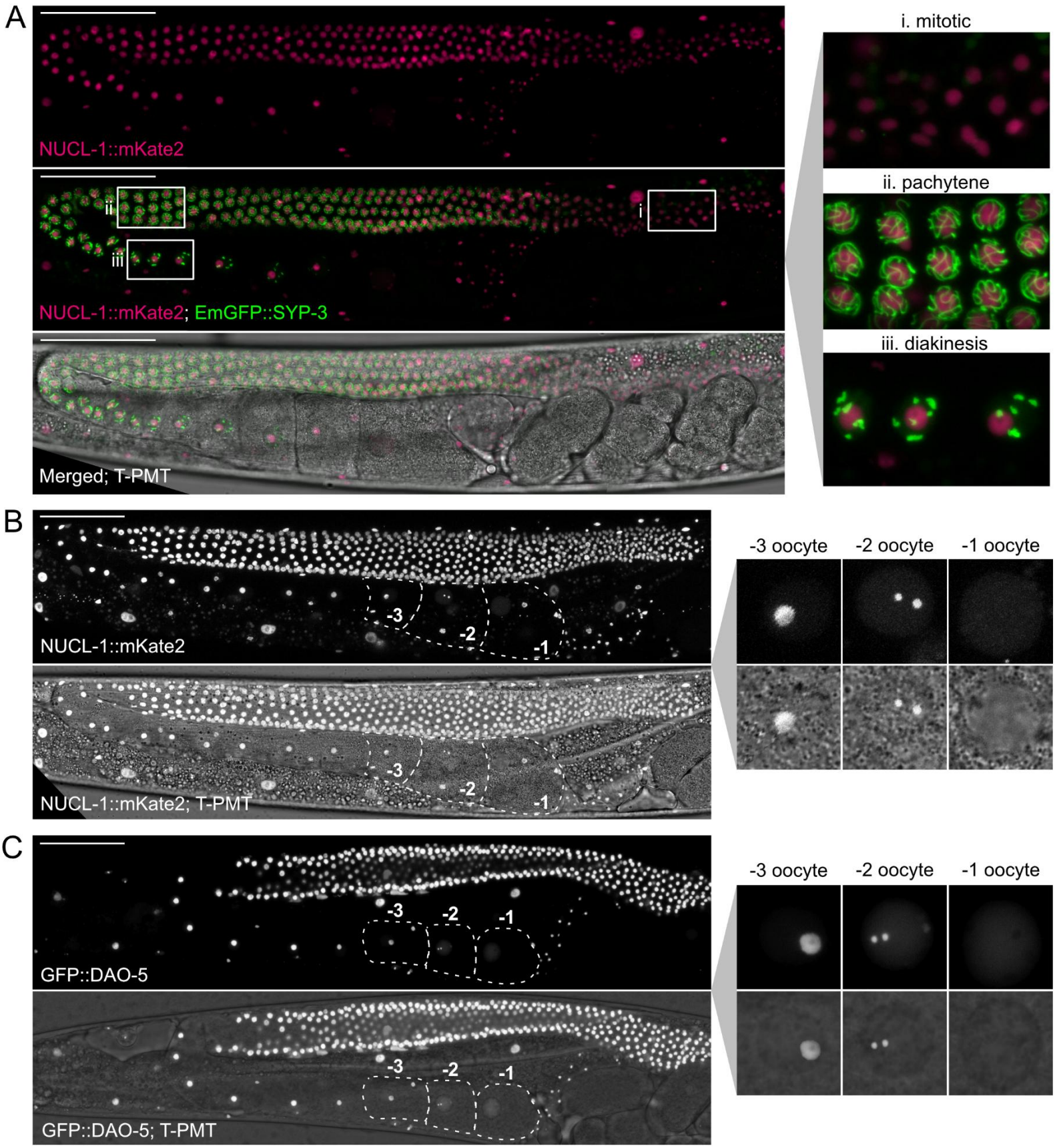

104

Figure 1. Nucleolar integrity remains intact during germ cell maturation until the penultimate mature oocyte. (A) 3-D confocal/T-PMT projection of an adult gonad arm with an endogenous NUCL-1::mKate2 nucleolar marker and an EmGFP::SYP-3 meiosis marker. Nucleoli are present throughout the mitotic, pachytene, and diakinesis zones, as indicated by the localization of EmGFP::SYP-3. Scale bar = 50 µm. **(B)** 3-D confocal/T-PMT projection of an adult gonad arm with an endogenous NUCL-1::mKate2 nucleolar marker. NUCL-1 forms droplets in the "-2" oocyte and is absent in the most proximal and mature "-1" oocyte. Scale bar = 50 µm. **(C)** 3-D confocal/T-PMT projection of an adult gonad arm with an endogenous GFP::DAO-5 nucleolar marker. Similar to NUCL-1, DAO-5 forms droplets in the "-2" oocyte and disappears entirely in the "-1" oocyte. Scale bar = 50 µm.

Disruption of RNA Pol I activity compromises nucleolar structure throughout the germline

Having established that a spherical nucleolus persists through most of germline development in mature hermaphrodites, we next asked how reducing rDNA transcription would affect its structure. Nucleolar integrity depends on robust RNA polymerase I (Pol I) activity, as the formation of nucleolar subcompartments and phase separation properties are largely driven by elevated concentrations of rRNA, along with its bound nucleolar factors [27,28,40]. Although prior work in the *C. elegans* germline utilized Actinomycin D to inhibit rDNA transcription, no visible disturbance of nucleolar structure was detected, likely because transcription was not suppressed below a critical threshold associated with nucleolar segregation [41,42]. Thus, to clearly disrupt nucleolar structure, we used the auxin-inducible degron (AID) system to substantially deplete RPOA-2, an endogenously tagged catalytic subunit specific to RNA Pol I, which is orthologous to human *POLR1B* [38,43].

Animals expressing degron::GFP::RPOA-2 were treated with 1 mM auxin (IAA) at the L4 stage for 18 hours, after which gonads from young adults were dissected and examined by fluorescent microscopy. A significant decrease in mean GFP intensity confirmed the near total depletion of RPOA-2 in germ cells (**Figure 2A left** and **S1A**, one-tailed Welch's two-sample *t*-test, $p < 2.2\times10^{-16}$). To confirm that this depletion impaired rDNA transcription, we performed RNA-seq on gonadal samples without polyA selection and quantified the abundance of reads mapping to two loci uniquely found in nascent pre-rRNA. We observed a significant decrease in reads mapping to the internally transcribed spacers (ITS1 and ITS2), indicating a considerable decrease in RNA Pol I activity (**Figure 2B top** and **S1B-C**, one-tailed Welch two-sample *t*-test, 4.6-fold average decrease for ITS1: $p = 0.021$, 1.6-fold average reduction for ITS2: $p = 0.0092$).

We next investigated whether these transcriptional reductions could sufficiently disrupt spherical nucleolar structure, identifiable by the formation of nucleolar caps [42]. In RPOA-2-depleted gonads, the nucleolar marker NUCL-1::mKate2, showed cap-like structures throughout the germline, in contrast to the more uniform spherical nucleoli in control animals (**Figure 2C**). This phenotype suggests that the threshold of rDNA transcription required for nucleolar integrity was not met upon RPOA-2 depletion, leading to a clear disruption of nucleolar morphology.

Although RPOA-2 depletion disrupts nucleolar structure by reducing rRNA synthesis, it also suspends ribosome production, which might impact the translational capacity of developing germ cells [43]. Despite the generally low transcriptional activity of germ cells, proper ribosome production is essential for translational regulation of gene expression and maternal ribosome loading to ensure embryonic viability

[44,22,45,46]. Importantly, our prior work indicates that both the depletion of RPOA-2 or ribosome assembly factors result in a comparable decrease in overall ribosome production, as evidenced by developmental arrest on auxin [43]. Thus, to separate the effects of nucleolar disruption from potential consequences of ribosome biogenesis disruption, we conducted identical experiments using an endogenous fluorescently-tagged AID strain for GRWD-1, a chaperone that guides RPL-3 assembly into the 60S ribosomal subunit [43,47].

Following auxin treatment of L4 animals, we observed a significant decrease in GRWD-1::degron::GFP intensity in germlines, confirming the depletion of GRWD-1 (**Figure 2A right** and **S1A**, one-tailed Welch's two-sample *t*-test, $p < 2.2\times10^{-16}$). However, RNA-seq analyses revealed no significant reduction in ITS1 and ITS2 pre-rRNA reads, suggesting that GRWD-1 depletion does not impair rRNA synthesis mediated by RNA Pol I activity (**Figure 2B bottom** and **S1B-C**, one-tailed Welch's two-sample *t*-test, 1.4-fold average increase in ITS1: $p = 0.99$, 1.4-fold average decrease in ITS2: $p = 0.16$). Instead, consistent with prior observations involving RPL-3 reduction, the ITS1 intermediate accumulated under GRWD-1 depletion (**Figure S1B**, [21]. Furthermore, the nucleolar morphology in GRWD-1-depleted germlines appeared vacuolated yet retained a persistent spherical form, similar to the morphology observed when RPL-3 is reduced (**Figure 2C**) [21]. Polysome profiling further indicates that global translation levels are similarly reduced under both RPOA-2 and GRWD-1 depletion (**Figure S1D**, RPOA-2: 38% reduction, GRWD-1: 41% reduction, data from [43]).

Together, these findings support the conclusion that although RPOA-2 and GRWD-1 depletion both reduce ribosome biogenesis, only impaired rRNA transcription, mediated by a disruption of RNA Pol I activity, disrupts spherical nucleolar structure throughout the germline. This result highlights a specific requirement for RNA Pol I activity in maintaining nucleolar morphology during oogenesis, independent of downstream ribosome assembly.

Figure 2

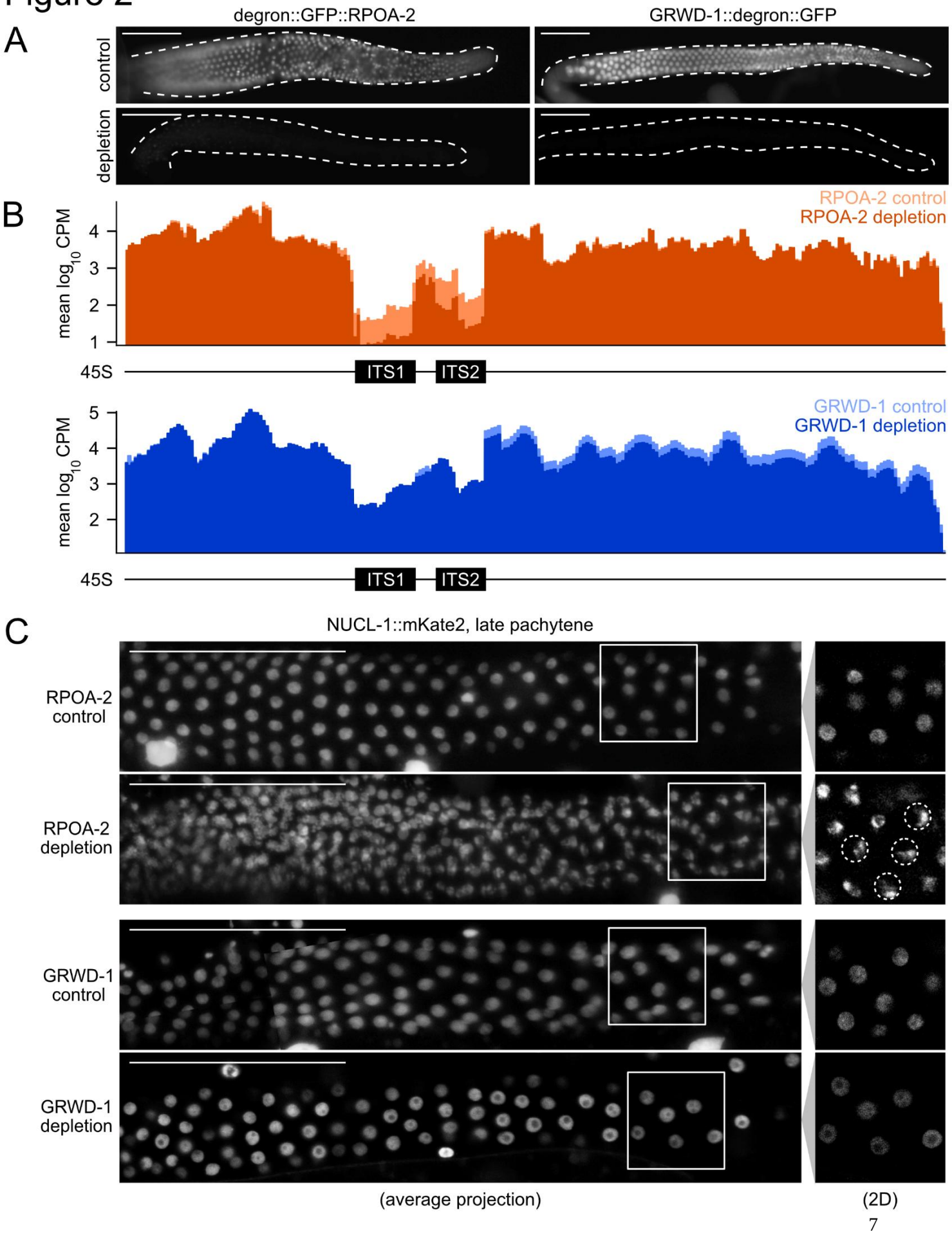

Figure 2. Reducing RNA Pol I activity, but not ribosome assembly, disrupts nucleolar structure in the germline. (A) Fluorescent images of degron::GFP::RPOA-2 and GRWD-1::degron::GFP in dissected gonads from young adults with 18 hours of control (EtOH) or 1 mM auxin (IAA) treatment at the L4 stage. Dotted lines indicate the outline of the gonad arm. Scale bar = 50 µm. **(B)** Average $\log_{10}$ counts per million (CPM) reads from gonadal RNA-seq (without polyA selection) mapped to a simplified single-copy 45S rDNA locus. Averages are composed of three biological replicates per condition, each consisting of 20 gonads. RPOA-2-depleted germlines show reduced coverage across internally transcribed spacer (ITS) regions compared to GRWD-1-depleted germlines. **(C)** Live 3-D confocal projection (left) of an endogenous NUCL-1::mKate2 nucleolar marker in the late pachytene zone of young adults treated with or without auxin to deplete degron::GFP::RPOA-2 or GRWD-1::degron::GFP. A zoomed-in 2-D layer (right) shows that nucleoli lose their spherical shape and form nucleolar caps (circled in white) after RPOA-2 depletion, whereas GRWD-1 depletion leads to vacuolar nucleoli formation with persistent spherical volume. Scale bar = 50 µm.

Supplementary Figure 1

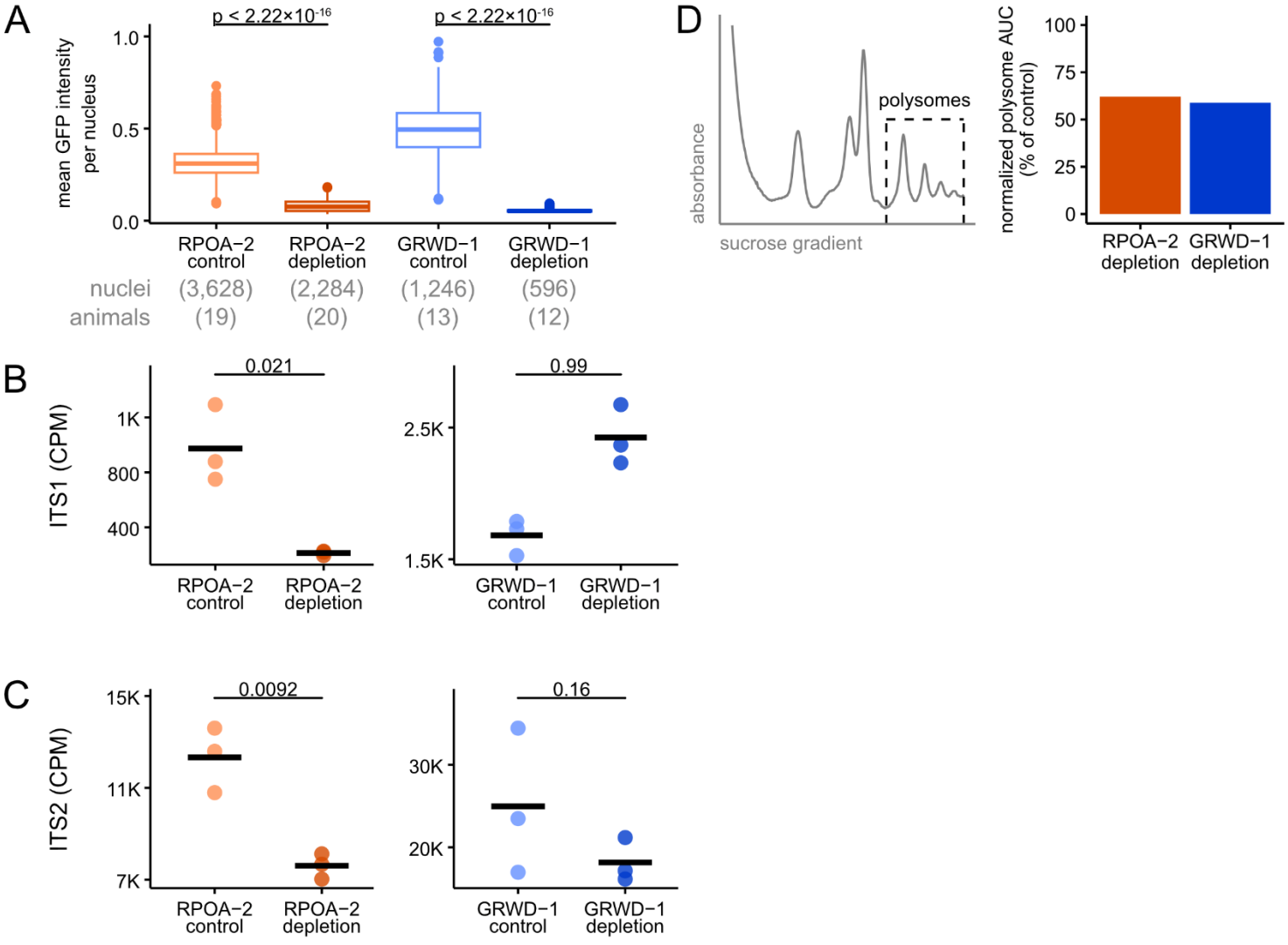

Figure S1. RPOA-2 depletion uniquely disrupts RNA Pol I activity, while reducing the translating pool of ribosomes to a similar extent as GRWD-1 depletion. (A) Distribution of degron::GFP::RPOA-2 or GRWD-1::degron::GFP signal intensity per nucleus from dissected gonads after 18 hours of control or auxin treatment at the L4 stage. Sample sizes are noted under the x-axis. **(B-C)** Comparisons of counts per million (CPM) reads across a simplified single copy of the **(B)** ITS1 locus and **(C)** ITS2 locus based on RNA-seq (without polyA selection) performed on dissected gonads after 18 hours of control or auxin treatment at the L4 stage. Each point represents a biological replicate, each consisting of 20 gonads. Cross bars represent the mean. **(D)** Example of a polysome profile, highlighting the polysome fraction used for quantification (left). Area under the curve (AUC) of polysome fraction (normalized to AUC of free RNA) from L4 animals after 24 hours of control or auxin treatment to deplete RPOA-2 or GRWD-1 (right). The fraction of translating ribosomes is similarly reduced after depleting RPOA-2 and GRWD-1. All comparisons were performed using a one-tailed Welch's two-sample *t*-test between control and auxin samples.

RNA Pol I activity plays a ribosome-biogenesis-independent role in maintaining oocyte production and morphology

To investigate whether germ cells remain viable when RNA Pol I activity is reduced, we stained control and RPOA-2-depleted animals with acridine orange to label cell corpses. After 18 hours of control or depletion treatment, the number of cell corpses in RPOA-2-depleted germlines did not differ significantly from controls (**Figure S2A-B**, two-tailed Welch's two-sample t-test, p = 0.22), suggesting that apoptosis was not induced during this time frame. Given that germ cells remained viable, we next examined how RPOA-2 or GRWD-1 depletion influenced germline maturation by measuring proximal arm length, the number of proximal oocytes, and the dimensions of the three most proximal oocytes. We also normalized proximal arm length to overall body area, given that the global AID system can reduce body size due to high basal degradation in the absence of auxin, particularly in the GRWD-1 AID strain [43] (**Figure S2C**, one-tailed Welch's two-sample *t*-test with Bonferroni correction, RPOA-2: $p = 0.00041$, GRWD-1: $p = 0.0013$).

A principal component analysis of these measurements showed that GRWD-1-depleted animals clustered closely with their controls, whereas RPOA-2-depleted animals clustered farther from their controls, indicative of distinct morphological differences specific to RPOA-2 depletion (**Figure 3B**). Indeed, the ratio of the proximal arm length to body area was reduced only in RPOA-2-depleted animals (**Figure 3C**, two-tailed Welch's two-sample *t*-test with Bonferroni correction, RPOA-2: $p = 0.054$, GRWD-1: $p = 0.75$). Similarly, RPOA-2 depletion uniquely diminished the number of proximal oocytes (**Figure 3D**, two-tailed Welch's two-sample *t*-test with Bonferroni correction, RPOA-2: $p = 5.6 \times 10^{-11}$, GRWD-1: $p = 1$) and caused the three most proximal oocytes to occupy a significantly larger fraction of the proximal arm (**Figure 3E**, two-tailed Welch's two-sample *t*-test with Bonferroni correction, RPOA-2: $p < 0.05$, GRWD-1: $p > 0.05$). These results suggest that oocyte production and morphology are disrupted specifically by reducing RNA Pol I activity, rather than by impairing ribosome assembly.

Supplementary Figure 2

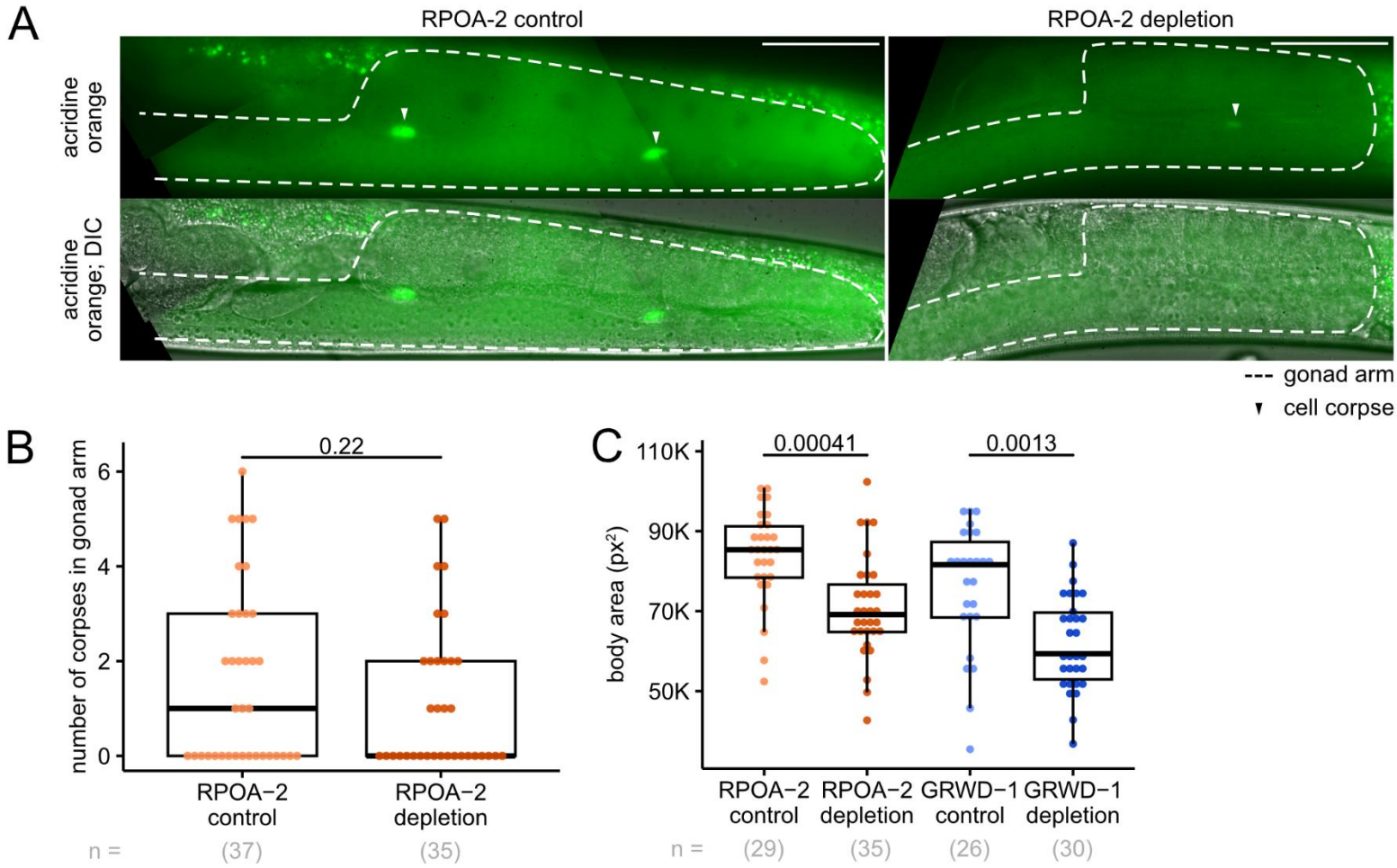

Figure S2. Effects of reduced RPOA-2 or GRWD-1 activity on germline cell death and body area. **(A)** Representative images of acridine-orange-stained germlines after 18 hours of control treatment or RPOA-2 depletion. Cell corpses are indicated by white triangles, and gonad arms are outlined in white. Scale bar = 50 μm. At this time point, RPOA-2-depleted germlines have similar amounts of proximal cell corpses as control germlines. **(B)** Distribution of cell corpses per gonad arm based on acridine orange staining. Each point represents the number of corpses in a gonad arm, and *n* represents the number of gonad arms across three biological replicates. A two-tailed Welch's two-sample *t*-test suggests that the average number of cell corpses in control and RPOA-2-depleted germlines are not distinguishable. **(C)** Distribution of body areas after 18 hours of control or auxin treatment. Each point represents measurements from an individual worm, and *n* represents the total number of worms per condition. A one-tailed Welch's two-sample *t*-test with Bonferroni correction supports that reducing RNA Pol I activity and ribosome assembly both decrease the size of the organism relative to respective controls.

Figure 3

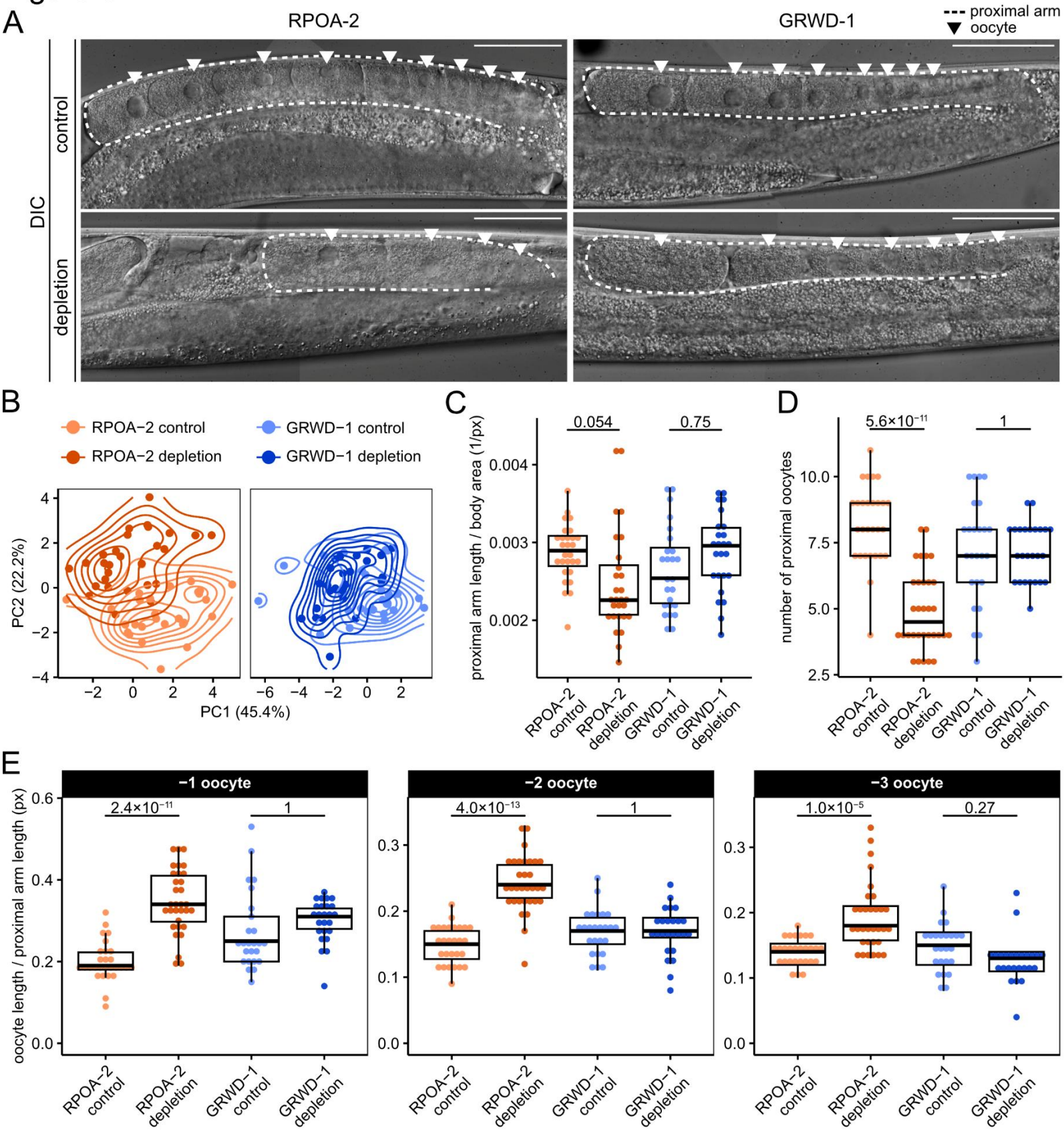

Figure 3. Oocyte morphology and organization are impaired by reduced RNA Pol I activity, independent from RNA Pol I's role in ribosome production. (A) Representative DIC images of adult germlines after 18 hours of control or auxin treatment. The dotted line highlights the proximal arm, and arrows point to proximal oocytes. Scale bar = 50 μm. **(B)** Principal component analysis and density contour estimates of various animal and gonadal measurements (body area, length of the proximal arm, length and area of the three most proximal oocytes, and the number of proximal oocyte counts). Each point represents an individual worm. RPOA-2-depleted germlines cluster more distinctly from their controls compared to GRWD-1-depleted germlines. **(C)** Distribution of the ratios of proximal arm length to body area in adult germlines after 18 hours of control or auxin treatment. When accounting for body area, germlines developing under reduced RNA Pol I activity have smaller proximal arms relative to their controls, while germlines developing under similarly reduced levels of ribosome production show an insignificant difference in proximal arm size relative to their controls. **(D)** Distribution of the number of proximal oocytes in adult germlines after 18 hours of control or auxin treatment. The smaller proximal arm size observed in RPOA-2-depleted germlines is explained by a reduction in the number of proximal oocytes compared to controls. **(E)** Distribution of the ratio of oocyte length to proximal arm length for the three most proximal oocytes ("-1", "-2", "-3") in adult germlines after 18 hours of control or auxin treatment. The three-most proximal oocytes of RPOA-2-depleted germlines occupy a significantly larger proportion of the proximal arm length compared to their controls, suggesting that oocyte morphology is significantly altered by reducing RNA Pol I activity. Each point in **(C-E)** represents a measurement from an individual animal. All comparisons were performed using two-tailed Welch's two-sample *t*-tests followed by Bonferroni correction, and are based on measurements from the following number of animals: RPOA-2 control = 29, RPOA-2 depletion = 35, GRWD-1 control = 26, GRWD-1 depletion = 30.

Disruption of RNA Pol I induces meiotic chromosome abnormalities, mediated by nucleolar caps rather than ribosome biogenesis

The observation that reduced RNA Pol I activity, but not impaired ribosome assembly, leads to defects in oocyte maturation prompted us to investigate how each condition affects meiotic progression. Using a SPY555-DNA probe, we determined whether germ cells adopted characteristic DNA morphology in the mitotic, transition, and meiotic zones. We assessed the appearance of crescent shaped nuclei in the transition zone, where DNA clusters near one nuclear pole, and whether chromosomes in the meiotic zone were repositioned to the nuclear periphery.

Following either control or 1 mM auxin (IAA) treatment of RPOA-2 and GRWD-1 AID strains, we observed that both depletions disrupted grid-like organization within the gonadal sheath and syncytia, seen in controls (**Figure 4A, right**). Despite this overall spatial disorganization, GRWD-1-depleted gonads still displayed crescent shaped nuclei in the transition zone—though spanning a shorter region—and exhibited homolog pairs at the nuclear periphery in the meiotic zone (**Figure 4A, right**), suggesting that reduced ribosome production does not grossly affect meiotic progression. In contrast, RPOA-2-depleted gonads showed fewer germ cells with crescent shaped chromosomes and less obvious pairing, making it difficult to determine whether the chromosomes were at the nuclear periphery (**Figure 4A, right**).

These differences raised the possibility that nucleolar integrity is critical for proper chromosome morphology during meiotic entry. Specifically, transition zone nuclei move the nucleolus and the chromosomes to opposite poles, likely to bring homologs into proximity [48–50]. After a certain threshold of RNA Pol I activity loss, nucleolar subcompartments can reorganize into caps (**Figure 2C**, **Figure 4A, left**) [51]. To test whether meiotic chromosome defects stem from nucleolar caps, we titrated auxin to generate a range of RNA Pol I activity levels and examined nucleolar and chromosomal structures. At 0.5 µM IAA, degron::GFP::RPOA-2 intensity was reduced by ~35% (**Figure 4B**), but nucleolar localization (NUCL-1::mKate2) (**Figure 4C, column 1**), transition zone chromosome morphology (**Figure 4C, column 3**), and meiotic chromosome morphology (**Figure 4C, column 4**) remained similar to controls. At 10 µM IAA, degron::GFP::RPOA-2 levels dropped by ~70% (**Figure 4B**), accompanied by pronounced nucleolar vacuoles (**Figure 4C, column 1**), crescent-shaped DNA (**Figure 4C, column 3**), and chromosomes pairing at the nuclear periphery (**Figure 4C, column 4**), though these paired chromosomes appeared more proximally than in gonads treated with 0.5 µM IAA.

Lastly, 500 µM IAA achieved a ~90% reduction of degron::GFP::RPOA-2 (**Figure 4B**), which was sufficient to induce nucleolar caps (**Figure 4C, column 1**), fewer definitively crescent shaped nuclei (**Figure 4C, column 3**), and some nuclei with paired chromosomes, again located more proximally (**Figure 4C, column 4**). These observations support the conclusion that abnormal meiotic chromosome morphologies emerge once nucleolar caps form, indicating that RNA Pol I activity and hence nucleolar integrity play a key role in regulating chromosome structure independently of ribosome production.

Figure 4

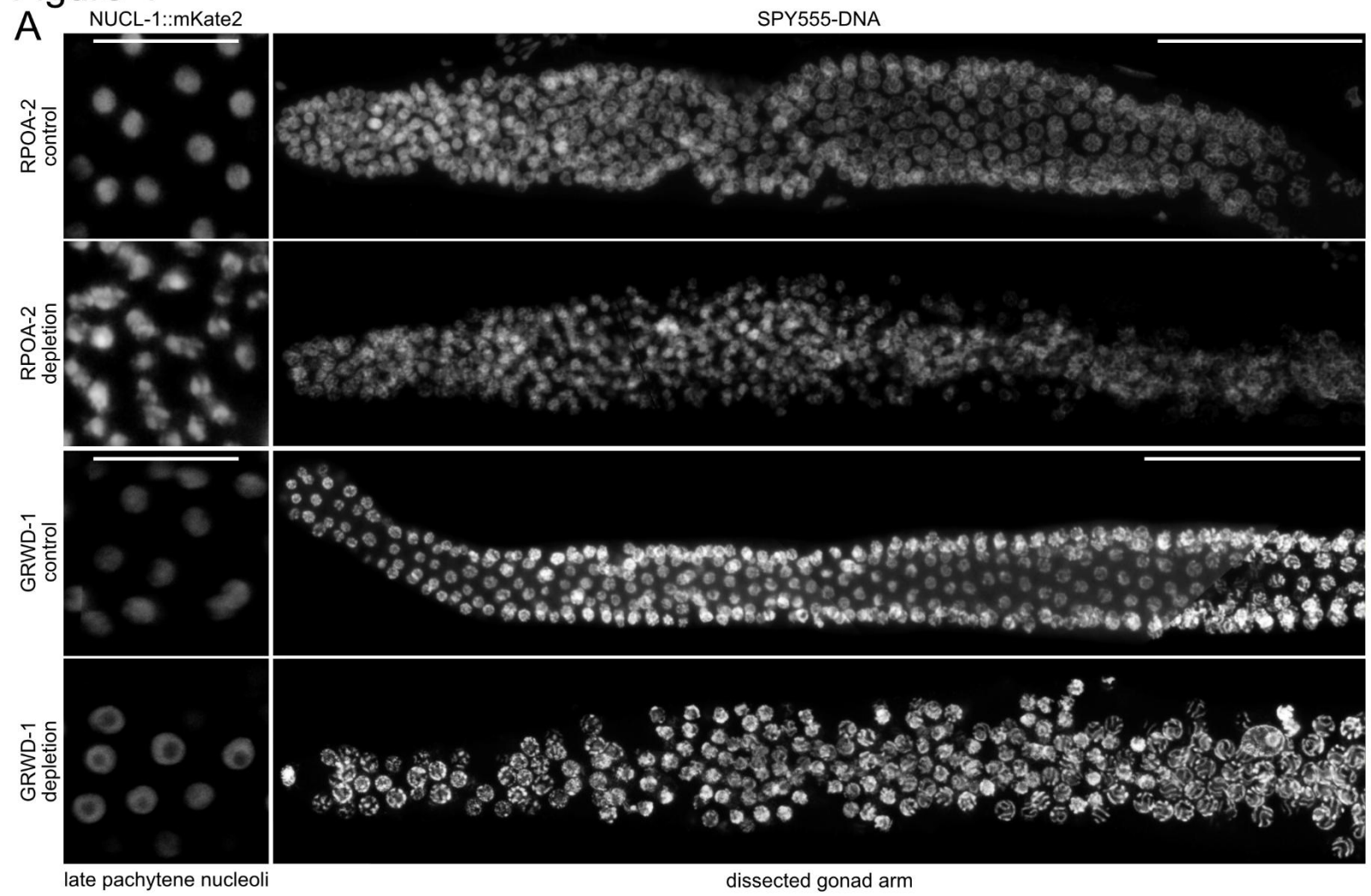

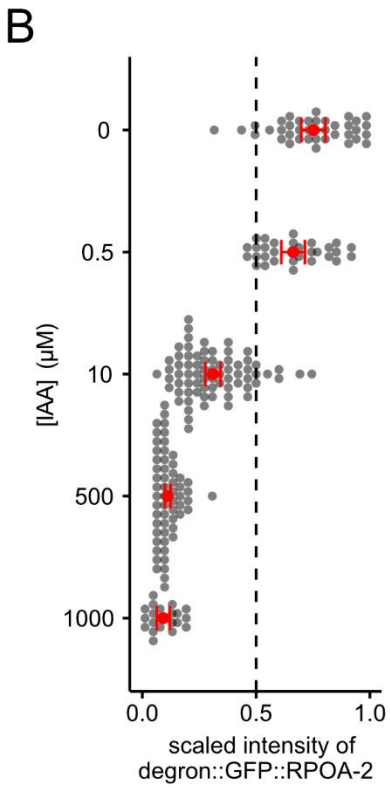

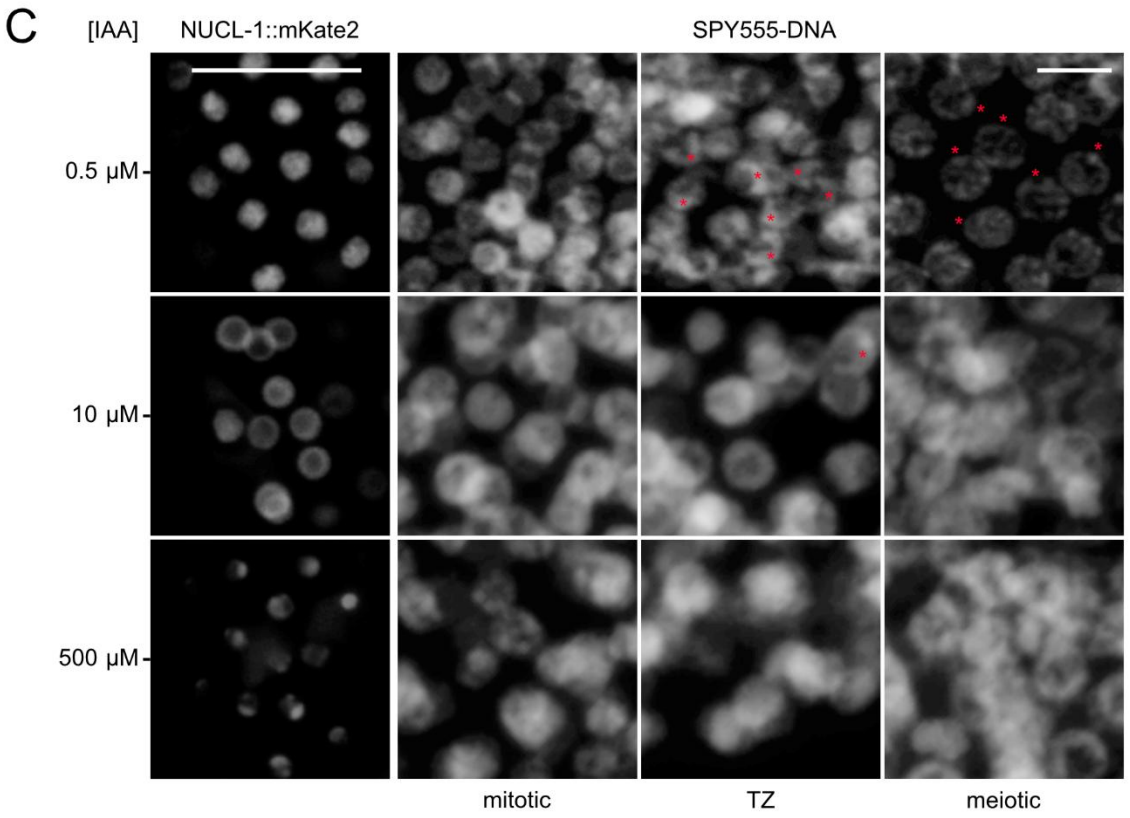

Figure 4. Irregular chromosome morphology during meiotic entry is nucleolar-cap dependent and independent from reduced ribosome assembly. (A) 3-D confocal average projections of late pachytene nucleoli identifiable by endogenously tagged NUCL-1::mKate2 (left), along with average projections of dissected gonad arms with a SPY555-DNA probe (right). Images were taken following control or 1 mM auxin (IAA) treatment to deplete RPOA-2 or GRWD-1. Left scale bar = 15 μm, right scale bar = 50 μm. **(B)** Effects of auxin concentration [IAA] on mean gonadal degron::GFP::RPOA-2 intensity (left). Intensity scaled with 0 μM treated maximum set to 1, and 1000 μM treated minimum set to 0. The mean and 95% confidence intervals for each distribution are represented in red, and each point represents the mean intensity measurement from a gonad. Sample sizes are 39, 31, 72, 58, and 23 gonads for 0, 0.5, 10, 500, and 1000 μM treatments, respectively. **(C)** Live 3-D confocal projection of an endogenous NUCL-1::mKate2 nucleolar marker in late pachytene nucleoli of young adults treated with varying concentrations of auxin (IAA) to deplete RPOA-2 (column 1). Scale bar = 15 μm. Zoomed in representative nuclei within the mitotic, transition zone (TZ), or meiotic germline zones, imaged from dissected adult gonad arms with a SPY555-DNA probe after varying concentrations of auxin (IAA) treatment to deplete RPOA-2 (columns 2-4). Scale bar = 5 μm. Asterisks highlight nuclei with typical TZ or meiotic chromosome morphology.

Autosomal oogenesis gene promoters are more accessible after disrupting nucleolar structure

Given that nucleolar cap formation was associated with germline chromosome abnormalities, we next investigated whether specific genomic regions were preferentially affected by a reduction of RNA Pol I activity compared to reduced ribosome assembly. We performed ATAC-seq on dissected gonads from control and RPOA-2- and GRWD-1-depleted young adults. In RPOA-2-depleted germlines, 1,616 genomic regions were significantly more accessible (SMA), whereas only 99 regions were significantly less accessible (DESeq2, Benjamini-Hochberg adjusted $p < 0.05$). In GRWD-1-depleted germlines, 53 regions were more accessible and only one region showed reduced accessibility (DESeq2, Benjamini-Hochberg adjusted $p < 0.05$). Additionally, 41 regions were SMA in both RPOA-2- and GRWD-1-depleted gonads (**Figure 5A**).

To functionally interpret these changes, we annotated each ATAC-seq peak to its nearest genomic feature, and found that more than 80% of SMA peaks in either RPOA-2- or GRWD-1-depleted germlines were located within 1 kb of the promoter of the nearest gene, compared to only 50% in background peaks (**Figure 5B**). Moreover, SMA regions in RPOA-2-depleted germlines were concentrated on autosomes (**Figure 5C**), with ~2-7% of peaks per autosome showing increased accessibility, compared to only ~0.2% on the X chromosome (**Figure 5C**). In GRWD-1-depleted germlines, SMA regions on the X chromosome were also less prominent, though to a lesser extent (**Figure S3A**). Overall, these results indicate that nucleolar disruption caused by reduced RNA Pol I activity leads to a more pronounced increase in chromatin accessibility at autosomal promoters, emphasizing the role of nucleolar integrity in genome organization.

Figure 5

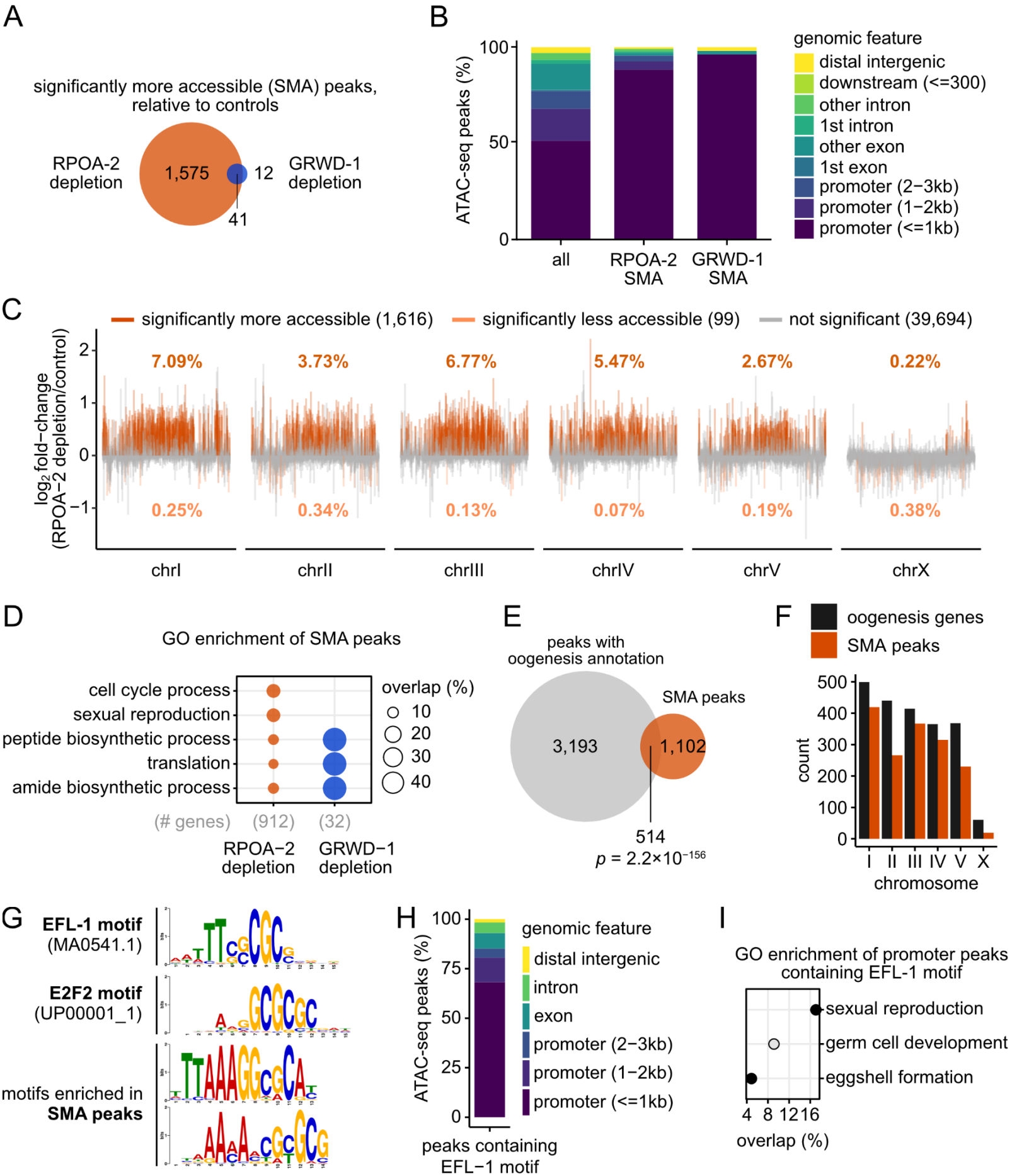

Figure 5. Disrupting RNA Pol I activity prematurely primes autosomal promoters in an accessible state associated with oogenesis. (A) Venn diagram comparing the number of significantly more accessible (SMA) regions following RPOA-2 depletion versus GRWD-1 depletion, based on an adjusted $p < 0.05$. **(B)** Genomic feature annotations of ATAC-seq peaks. Regions with significantly increased accessibility after RPOA-2 or GRWD-1 depletion are predominantly located within 1 kb of the nearest promoter. (SMA = significantly more accessible). **(C)** Log_2 fold-change estimates of chromatin accessibility based on gonadal ATAC-seq data from at least three biological replicates per condition, each composed of 20 gonads. Each segment along the x-axis represents a genomic region. The number of differentially accessible regions are noted in the plot legend based on an adjusted $p < 0.05$. Percentages represent the proportion of differentially accessible peaks relative to the total number of called peaks per chromosome. Depleting RPOA-2 increases autosomal chromatin accessibility, but does not affect the X chromosome. **(D)** Enrichment of gene ontology (GO) biological processes in genes exhibiting increased accessibility after depletion of RPOA-2 or GRWD-1 (Hypergeometric test, FDR < 0.001). The term "gene" refers to those associated with the nearest genomic feature annotation of each peak. Both reductions in RNA Pol I activity and ribosome assembly increase the accessibility of translation-related genes, while reducing RNA Pol I activity distinctly increases the accessibility of genes involved in biological processes such as sexual reproduction. **(E)** Overlap between peaks that are significantly more accessible (SMA) after RPOA-2 depletion and peaks near genes involved in oogenesis [52] (Hypergeometric test). **(F)** Chromosomal distribution of genes involved in oogenesis [52] and significantly more accessible (SMA) peaks after RPOA-2 depletion. **(G)** Alignment of the *C. elegans* EFL-1-binding site, human E2F-binding site, and the two motifs enriched in significantly more accessible (SMA) peaks after RPOA-2 depletion. **(H)** Genomic feature annotations of peaks containing an EFL-1-binding site. **(I)** GO enrichment analysis for biological processes among genes with promoter peaks that contain an EFL-1-binding site (Hypergeometric test, FDR < 0.05).

RNA Pol I-driven nucleolar disruption prematurely primes oogenesis promoters in an accessible state

Considering that nucleolar cap formation was linked to increased chromatin accessibility along the promoters of autosomal genes, we asked whether the genes affected by these accessibility changes contribute to the defective oocyte maturation that emerges specifically under reduced RNA Pol I activity. To examine this, we performed a differential gene ontology (GO) analysis of biological processes enriched in genes with increased accessibility following RPOA-2 or GRWD-1 depletion. Regions with increased accessibility following a reduction of RNA Pol I activity were enriched for sexual reproduction and cell cycle processes, including meiotic cell cycle, chromosome organization, and oogenesis (**Figure 5D** and **Table S2**, Hypergeometric test, FDR < 0.001). Additionally, RPOA-2 depletion uniquely increased the accessibility of genes that function both in germ/oocyte development and translation (e.g., *daz-1, fbf-2, fog-1, gld-1, glp-4, larp-1, mex-3, oma-1, oma-2*) (**Figure 5D** and **Table S2**, Hypergeometric test, FDR < 0.001). In contrast, depleting GRWD-1, which impairs ribosome assembly without disrupting spherical nucleolar structure, did not show enrichment of sexual reproduction processes in more accessible chromatin regions. Instead, genes related to translation, mostly consisting of ribosomal protein genes, mitochondrial-ribosome-related genes, and translation initiation/termination factors (e.g., *rps-0, rps-9, rps-17, rps-27, rpl-9, rpl-18, rpl-25.2, rpl-28, inf-1, larp-5, rack-1, W01D2.1*) showed increased accessibility under both RPOA-2 and GRWD-1 depletion, consistent with adaptive response to reduced ribosome production. These results suggest that although decreased ribosome production increases accessibility at translation related loci in both conditions, reducing RNA Pol I activity uniquely increases the accessibility of oogenesis genes, potentially contributing to the defective oogenesis phenotype (**Figure 3**).

We further investigated the extent to which oogenesis genes were affected by RNA Pol I depletion using a set of 2,177 genes with germline-enriched expression in feminized *fem-1(lf)* mutants [52]. Of the 3,707 peaks annotated to these oogenesis genes, we detected a significant enrichment within regions that became significantly more accessible after RPOA-2 depletion (**Figure 5E**, Hypergeometric test, $p = 2.2\times10^{-156}$). Consistent with this observation, the autosomal bias of oogenesis genes parallels the autosomal bias in accessibility observed for RPOA-2-depleted gonads (**Figure 5F**).

To assess potential regulators of these accessibility changes, we searched for enriched transcription factor (TF) binding motifs that gained accessibility after RPOA-2 depletion. Compared to ungapped sequence motifs present in background peaks, we identified eight motifs significantly enriched in the accessible peaks of RPOA-2-depleted germ cells (**Table S3**, STREME, $p < 0.05$, $E < 0.05$). We aligned the eight motifs enriched in RPOA-2-depleted germlines against the 842 TF motifs present in the TFBSshape database and identified 143 unique TF binding motif matches in peaks with increased accessibility after RPOA-2 depletion (Tomtom, $p < 0.05$, $E < 8.42$) [53]. After manual curation to combine redundant query motifs and their repeated matches, we found relatively few matches with visibly cohesive alignments to their query motifs. Notably, we identified four total hits to human E2F-binding sites from the enriched RTGCGCCTTTAAA and CGCRCGKTKTTTRN motifs (**Figure 5G**, **Table S3**), which are orthologs to the oogenesis-promoting *C. elegans* transcription factor EFL-1 [54]. Additionally, the CGCRCGKTKTTTRN motif aligned to the yeast Rsc3- and Rsc30-binding sites, which regulate ribosomal protein gene expression [55].

Although there was no enrichment of motifs for accessible regions following GRWD-1 depletion, we corroborated that the EFL-1-like binding motif was specifically more accessible following RPOA-2 depletion, but not after GRWD-1 depletion. We identified 242 ATAC-seq peaks containing a significant match to the EFL-1 motif, predominantly in promoters less than 1 kb from the nearest gene (**Figure 5H**, FIMO, $p < 0.0001$). Genes with promoter peaks containing an EFL-1 motif are involved in processes such as sexual reproduction, germ cell development, and eggshell formation (**Figure 5I**, Hypergeometric test, FDR < 0.05). Lastly, genes with a promoter peak containing the EFL-1 motif were not remodeled after reducing ribosome assembly, but did show increased accessibility after reducing RNA Pol I activity (**Figure S3F**).

We next examined whether these accessibility changes affected steady-state transcript levels by analyzing RNA-seq data from dissected gonads after RPOA-2 or GRWD-1-depletion. We identified 188 genes with increased mRNA levels and 177 genes with reduced mRNA levels upon RPOA-2 depletion (**Figure S3B**, Benjamini-Hochberg adjusted $p < 0.05$). Similarly, GRWD-1 depletion led to increased mRNA levels in 287 genes and decreased levels in 235 genes (**Figure S3B**, Benjamini-Hochberg adjusted $p < 0.05$). We did not observe significant functional GO enrichment in the over-expressed genes unique to RPOA-2 depletion (**Table S5**, Hypergeometric test, FDR < 0.001). Both conditions shared 57 over-expressed genes and 87 under-expressed genes with a shared enrichment of under-expressed genes related to translation (**Figure S3C-D**, Hypergeometric test, FDR < 0.001), mirroring patterns observed in chromatin accessibility. Moreover, we found no overall correlation between chromatin accessibility and mRNA levels for all genes or for those that were differentially accessible and differentially expressed (**Figure S3E**, $p > 0.05$).

Given the enrichment of a putative repressive Rsc30-like motif in accessible regions following RPOA-2 depletion, we hypothesized that translation-related genes would be under-expressed. Indeed, many ribosomal protein genes are significantly reduced after RPOA-2 depletion, consistent with negative regulation (**Figure S3G**, one-tailed one-sample *t*-test, alternative hypothesis: average $\log_2$ fold-change < 0, $p = 0.00020$). In contrast, genes related to sexual reproduction did not exhibit increased transcript levels, despite increased chromatin accessibility and the enrichment of a potential oogenesis-promoting transcription factor motif (**Figure S3G**, one-tailed one-sample *t*-test, alternative hypothesis: average $\log_2$ fold-change > 0, $p = 0.16$). In agreement, genes with a promoter peak containing an EFL-1 motif did not significantly increase mRNA expression after RPOA-2 depletion (**Figure S3F**, one-tailed one-sample *t*-test, alternative hypothesis: $\log_2$ fold-change > 0, $p = 0.14$). Thus, although oogenesis promoters become more accessible, mRNA levels remain unchanged, reflecting an oogenesis-specific chromatin state that is primed for but does not undergo productive transcription.

Together, these results suggest that decreasing RNA Pol I activity triggers nucleosome remodeling to reduce the expression of ribosomal proteins, potentially conserving resources in response to limited rRNA availability for ribosome biogenesis. However, this reduction in RNA Pol I activity also leads to nucleosome remodeling that increases the accessibility of oogenesis-related genes and oogenesis-promoting EFL-1 binding sites, potentially contributing to a defective oocyte maturation phenotype (**Figure 3**).

Supplementary Figure 3

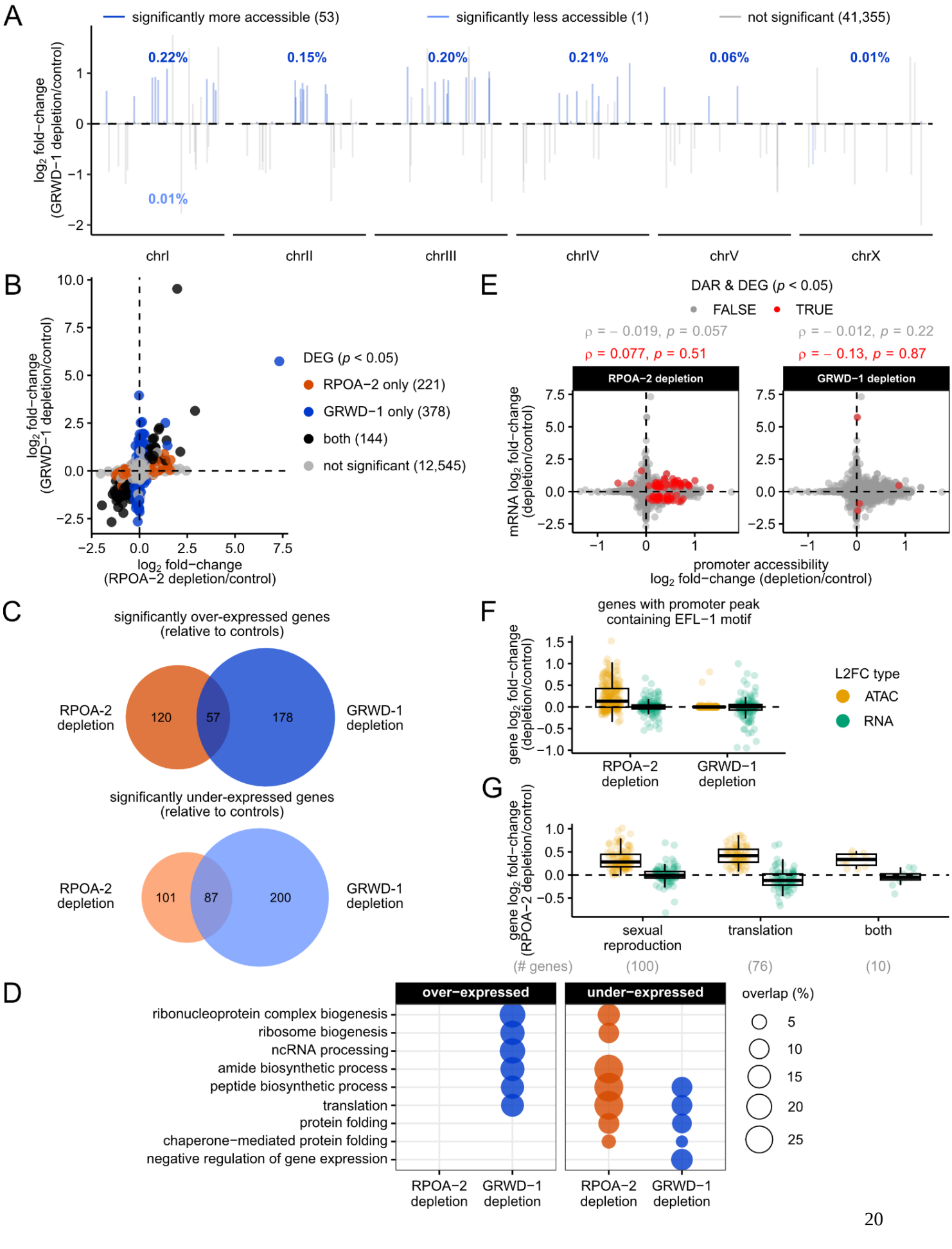

Figure S3. Chromatin and gene expression consequences following RPOA-2 and GRWD-1 depletion. **(A)** Log_2 fold-change estimates of chromatin accessibility based on gonadal ATAC-seq data from at least three biological replicates per condition, each composed of 20 gonads. Each segment along the x-axis represents a genomic region. The number of differentially accessible regions are noted in the plot legend based on an adjusted $p < 0.05$. Percentages represent the proportion of differentially accessible peaks relative to the total number of called peaks per chromosome. GRWD-1 depletion minimally increases chromatin accessibility in autosomal regions, and alters even fewer genomic regions compared to RPOA-2 depletion. **(B)** Log_2 fold-change estimates of gene expression from RNA-seq conducted on dissected gonads after RPOA-2 or GRWD-1 depletion. Biological replicates, consisting of 20 gonads: RPOA-2 control = 3, RPOA-2 depletion = 4, GRWD-1 control = 2, GRWD-1 depletion = 3. **(C)** Venn diagram to contextualize the difference in the scale of gene expression changes after RPOA-2 depletion compared to GRWD-1 depletion. **(D)** Enrichment of gene ontology biological processes in genes that were differentially expressed after RPOA-2 or GRWD-1 depletion (Hypergeometric test, FDR < 0.001). Both RPOA-2- and GRWD-1-depleted germ cells differentially expressed genes related to translation. **(E)** Log_2 fold-change estimates of promoter accessibility versus mRNA to investigate whether chromatin accessibility correlated with gene expression. We did not identify a significant correlation between promoter accessibility and mRNA levels across all genes (gray), or across genes that were both differentially accessible and differentially expressed after RPOA-2 or GRWD-1 depletion (black). **(F)** Comparison of ATAC-seq and RNA-seq log_2 fold-change estimates for genes with promoter peaks containing an EFL-1 motif after RPOA-2 or GRWD-1 depletion. On average, genes with a promoter EFL-1 motif did not show a significant increase in mRNA fold-changes after RPOA-2 depletion (one-tailed one-sample *t*-test, alternative hypothesis: log_2 fold-change > 0, $p = 0.14$). **(G)** Comparison of ATAC-seq and RNA-seq log_2 fold-change estimates in biological processes enriched in genes with increased chromatin accessibility after RPOA-2 depletion. Only the terms "sexual reproduction" and "translation" are represented, as they encompass the majority of related subprocesses. "Both" represents genes that are involved in both biological processes. On average, translation-related genes, including ribosomal proteins, have lower mRNA fold-changes after RPOA-2 depletion (one-tailed one-sample *t*-test, alternative hypothesis: average log_2 fold-change < 0, $p = 0.00020$), whereas genes related to sexual reproduction do not have significantly increased mRNA levels (one-tailed one-sample *t*-test, alternative hypothesis: log_2 fold-change > 0, $p = 0.16$).

Nucleolar-cap-dependent increases in chromatin accessibility are accompanied by a misregulation of H3K4 methylation associated with oogenesis

Throughout oogenesis, germ cells undergo extensive chromatin remodeling to prepare for meiotic chromosome condensation and subsequent zygotic genome activation (ZGA). One hallmark of this transition is the redistribution of H3K4me3 from gene bodies to promoters in mature oocytes [4]. Given that RPOA-2 depletion increases the accessibility of oogenesis-related regions, we asked whether these loci show typical signatures of H3K4me3 remodeling in maturing wild-type oocytes.

Genes undergoing H3K4me3 remodeling during oogenesis can be grouped into three clusters: Cluster 1 (strong H3K4me3 marks in both promoters and gene bodies), Cluster 2 (strong promoter-specific H3K4me3), and Cluster 3 (weaker promoter-specific H3K4me3) [4]. When we compared chromatin accessibility near genes in these clusters, we found that accessibility near oogenesis-specific H3K4me3 remodeled genes significantly increased after RPOA-2 depletion relative to a random set of regions (**Figure 6A**, Bonferroni-corrected one-tailed Welch's two-sample *t*-tests, $p < 0.05$). Consistent with the germ-to-oocyte H3K4me3 remodeling pattern, Cluster 1 genes showed increased chromatin accessibility along both promoters and gene bodies (**Figure 6B**, top). Cluster 2 genes exhibited increased accessibility mainly in promoters, while Cluster 3 genes displayed weaker promoter specific increases following RPOA-2 depletion (**Figure 6B**, middle and bottom).

Although reducing RNA Pol I activity shows signatures of H3K4me3 remodeling, changes in chromatin accessibility can also reflect the remodeling of other histone marks. We compared the abundance of three such histone marks—remodeled active H3K4me3, non-remodeled active H3K36me3, and non-remodeled repressive H3K27me3—within regions that became more accessible after RPOA-2 depletion, using available ChIP-seq data from wild-type germ cells and oocytes [56–58]. In wild-type germ cells, H3K27me3 marks were less abundant in SMA regions compared to random regions (**Figure 6C**, top left), while active marks (H3K36me3 and H3K4me3) were enriched in SMA regions (**Figure 6C**, top middle and right). In wild-type oocytes, we expected highly accessible regions after RPOA-2 depletion to show specific enrichment for H3K4me3, reflecting germ-to-oocyte histone remodeling. In agreement, H3K4me3 marks were enriched in SMA regions relative to random regions (**Figure 6C**, bottom right), while H3K27me3 and H3K36me3 signals were weak in both accessible and random regions (**Figure 6C**, bottom left and middle).

Since more than 80% of SMA peaks are near promoters (**Figure 5B**), and H3K4me3 marks shift to promoters in oocytes, we hypothesized that H3K4me3 signal would peak at the center of SMA regions in wild-type oocytes. In contrast, we expected H3K4me3 in wild-type germ cells to decrease around SMA regions, since H3K4me3 is typically present along gene bodies in germ cells. This pattern was confirmed, with H3K4me3 signal peaking in SMA regions relative to a random set of promoters in wild-type oocytes (**Figure 6D**, right), and decreasing around SMA regions in wild-type germ cells. H3K27me3 and H3K36me3 signals did not notably peak near SMA regions in either germ cells or oocytes (**Figure 6D**, left and middle). Our findings support that reducing RNA Pol I activity throughout the germline specifically increases the accessibility of promoters that are remodeled during the germ-to-oocyte transition through H3K4me3 deposition, suggesting that the spatiotemporal regulation of H3K4 methylation is misregulated under RNA Pol I-mediated nucleolar disruption.

In wild-type animals, H3K4 methylation progressively increases towards the proximal region of the gonad, and this spatial regulation of H3K4 methylation is essential for proper germline maturation [12,59]. Given that RPOA-2 depletion increases the accessibility of oogenesis-associated H3K4me3 regions and specifically disrupts oogenesis, we anticipated that the spatial regulation of H3K4 methylation would be altered in response to RPOA-2 depletion, likely through premature H3K4me3 deposition in accordance with increased chromatin accessibility. To investigate this, we performed gonadal H3K4me3 immunostaining and cell-segmentation image analysis to assess how reduced RNA Pol I activity affects changes in the deposition of H3K4me3 from the distal to proximal end of the gonad (**Figure 6E**, n = 50 control gonads with 3,933 cells, n = 77 depletion gonads with 8,134 cells). Individual germ cell positions were projected onto a linear gonad axis to evaluate how H3K4me3 immunostaining intensity correlated with cell position along the distal-proximal gonad axis (termed cell gonad position from here on) (**Figure 6F**, see Methods).

As expected, an aggregate analysis of cells from all control gonads revealed a significant gradual increase in H3K4 methylation along the distal-proximal axis, evidenced both by H3K4me3/DAPI normalized intensity (**Figure 6G, top**, Spearman coefficient = 0.41) and by per-gonad scaled H3K4me3 intensity (**Figure 6G, bottom**, Spearman coefficient = 0.36). Similarly, we also analyzed this positive H3K4me3 gradient within individual gonads and observed that the majority (84%) of control gonads had significant correlations between cell gonad position and normalized H3K4me3/DAPI intensity (**Figure 6H**, mean Spearman coefficient: 0.46±0.03, Benjamini-Hochberg adjusted p-value < 0.05), and also per-gonad scaled H3K4me3 intensity (**Figure 6H**, mean Spearman coefficient: 0.36±0.03, 78% with Benjamini-Hochberg adjusted p-value < 0.05). These results support that typical oogenesis is consistently associated with a moderate but important positive H3K4me3 gradient.

Under reduced RNA Pol I activity, the aggregated correlation between cell gonad position and H3K4me3 was reduced by approximately half, both relative to normalized H3K4me3/DAPI and per-gonad scaled H3K4me3 intensity (**Figure 6G**, Spearman coefficient = 0.26 and 0.14 for H3K4me3/DAPI and per-gonad scaled H3K4me3, respectively). Additionally, only 64% of RPOA-2-depleted gonads had significant, but weaker, correlations between cell gonad position and normalized H3K4me3/DAPI intensity (**Figure 6H**, mean Spearman coefficient: 0.23±0.04, Benjamini-Hochberg adjusted p-value < 0.05) and also per-gonad scaled H3K4me3 intensity (**Figure 6H**, mean Spearman coefficient: 0.12±0.03, 52% with Benjamini-Hochberg adjusted p-value < 0.05).

Lastly, compared to control gonads, RPOA-2-depleted gonads had a significant reduction in average correlation between cell gonad position and H3K4me3 (**Figure 6H**, one-tailed Welch's two-sample t-test, H3K4me3/DAPI: Benjamini-Hochberg adjusted p-value = 3.0×10^{-5}, per-gonad scaled H3K4me3: Benjamini-Hochberg adjusted p-value = 4.6×10^{-7}). Interestingly, this misregulation of H3K4me3 deposition could be explained by increased H3K4me3 in the distal region (**Figure 6G, top**).

Together, our data support that reducing overall RNA Pol I activity leads to premature ectopic promoter H3K4me3 deposition in oogenesis-related genes, contributing to aberrant chromatin states and defective oogenesis.

Figure 6

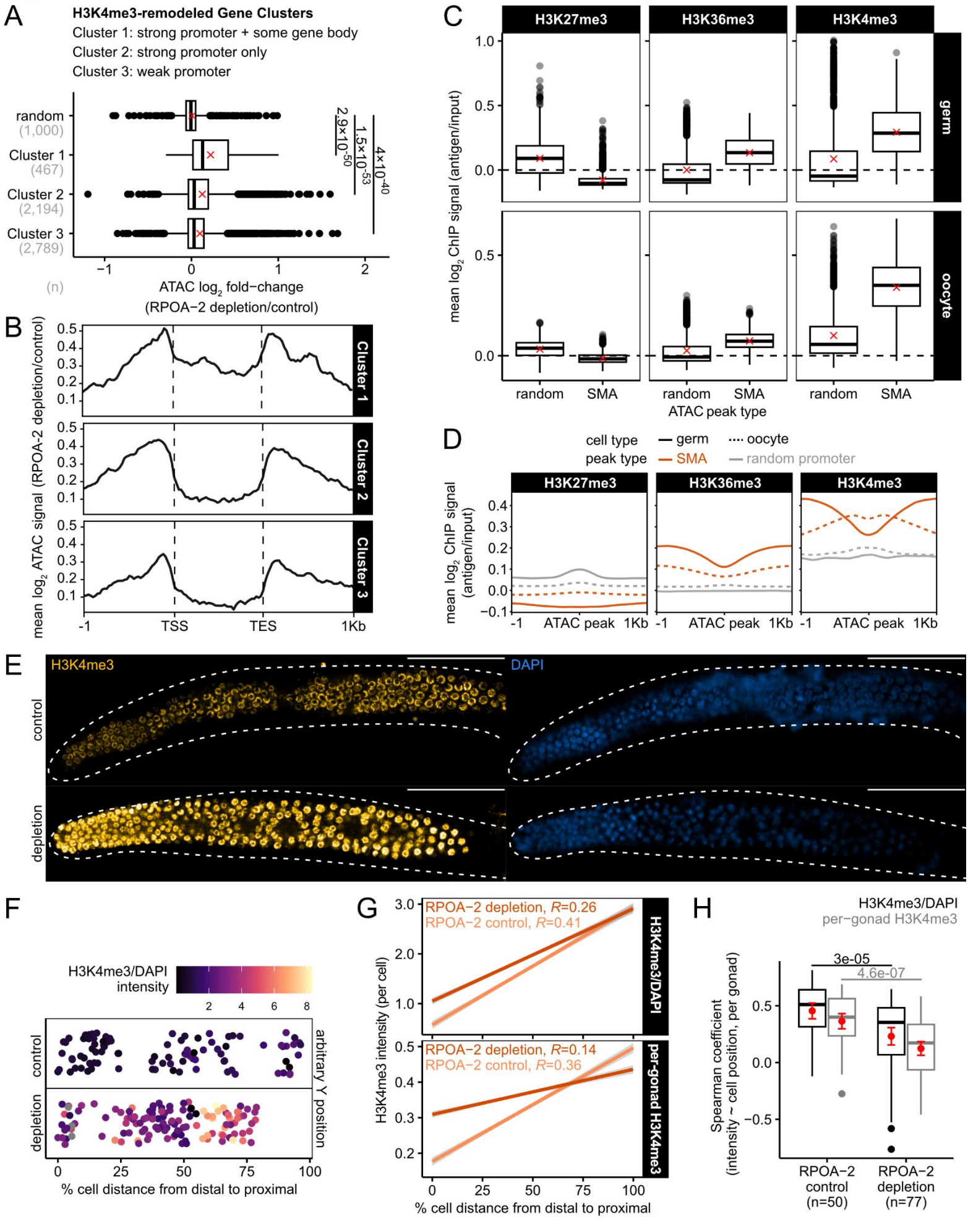

Figure 6. Chromatin regions that become more accessible after reducing RNA Pol I activity display patterns of H3K4me3 remodeling characteristic of the germ-to-oocyte transition. (A) Log_2 fold-change estimates of chromatin accessibility after RPOA-2 depletion in a random set of peaks, along with peaks annotated to genes that undergo H3K4me3 remodeling during oogenesis. The number of peaks in each set is specified by *n*, and means are denoted by an *x*. One-tailed Welch's two-sample *t*-tests with Bonferroni corrections were performed to test whether the average accessibility of regions near H3K4me3-remodeled genes is greater than the accessibility of a random set of regions in RPOA-2-depleted germlines. **(B)** Metagene analysis of mean log_2 ATAC signal (RPOA-2 depletion/control) within 1 kb of genes that undergo H3K4me3 remodeling during oogenesis. In gonads with reduced RNA Pol I activity, the shape of chromatin accessibility signal within each cluster mirrors the shape of H3K4me3 remodeling associated with each gene cluster. **(C)** Distribution of average H3K27me3, H3K36me3, and H3K4me3 ChIP signals from wild-type germ cells or oocytes within ATAC-seq peaks that are significantly more accessible (SMA) after RPOA-2 depletion, compared to signals within an identically-sized random subset of regions. Means are denoted by an *x*. **(D)** Metagene plot displaying the average H3K27me3, H3K36me3, and H3K4me3 ChIP coverage from wild-type germ cells or oocytes within 1 kb of genomic regions that are significantly more accessible (SMA) after RPOA-2 depletion, compared to coverage within an identically-sized random subset of promoter ATAC-seq peaks that are not SMA. **(E)** Representative 3-D confocal projections of adult gonad arms with H3K4me3 immunostaining and DAPI after control treatment or RPOA-2 depletion. Dotted lines represent gonad boundaries determined from T-PMT. Scale bar = 50 μm. **(F)** Using the example gonads from (E), we show germ cell position along a linear gonad axis following implementation of a gonad linearization algorithm (see Methods). Each point represents a germ cell detection; however, note that not all gonadal cells are detected by the algorithm. The distal tip is represented by zero on the gonad axis, whereas the most proximal tip of the gonad is variable based on biological size, gonad disruption during immunostaining, or gonad placement on Z-plane. H3K4me3 intensity measurements are normalized to DAPI to account for differences in permeability across gonads. **(G)** Linear relationship between germ cell position along the gonadal axis (from distal to proximal end) and H3K4me3 signal intensity (relative to DAPI intensity or scaled per-gonad), aggregated across all gonads. Spearman correlation coefficients are represented on the plot. Linear models and overall correlations are based on data from 3,933 control cell detections and 8,134 depletion cell detections from 50 and 77 gonads, respectively. **(H)** Distribution of Spearman coefficients estimating per-gonad positive correlations between cell position on the gonad axis and H3K4me3 intensity (relative to DAPI intensity or scaled per-gonad). Mean and standard error are represented by red points and crossbars. The number of gonads analyzed per condition are represented by *n*. A one-tailed Welch's two-sample *t*-test suggests that on average, control gonads have a higher magnitude correlation than gonads with reduced RNA Pol I activity (Benjamini-Hochberg adjusted *p*-values).

Supplementary Figure 4

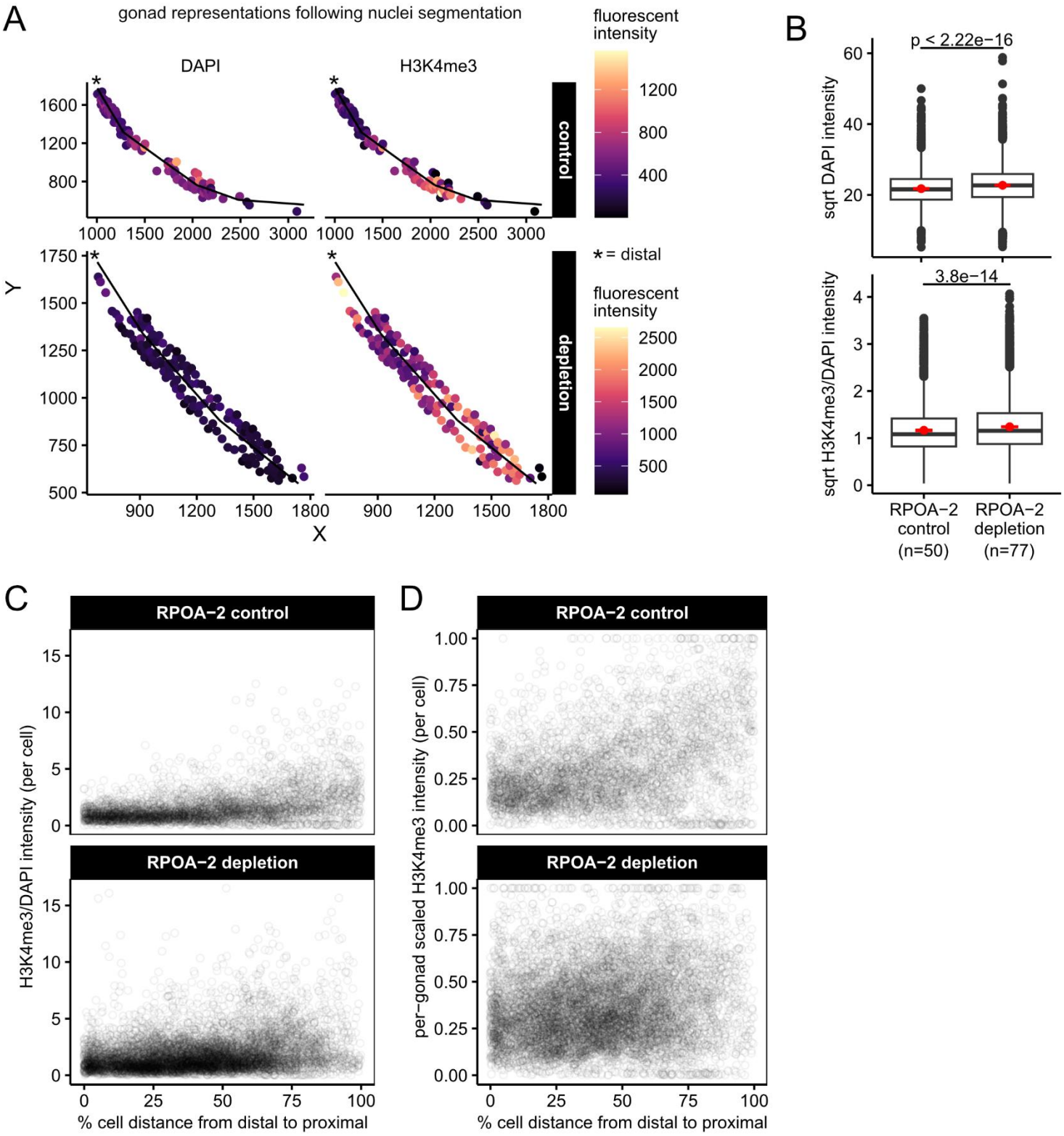

567

Figure S4. Examples of gonad linearization and fluorescent intensity measurements from gonadal samples immunostained with an anti-H3K4me3 primary antibody and Alexa Fluor™ 633 secondary antibody. (A) Using the representative gonads from Figure 6E, we show DAPI and H3K4me3 fluorescent intensity measurements following nuclei segmentation. Note that not all gonadal cells are detected by the algorithm (see Methods). Each point represents a germ cell detection located on 2D image coordinates prior to gonad linearization (shown in Figure 6F). The gonad skeleton used for linearization is represented by black line segments, and the distal tip is denoted with an asterisk. **(B)** Distributions of DAPI (top) and H3K4me3/DAPI (bottom) fluorescent intensity measurements from RPOA-2 control and depletion gonads. Mean and standard error are represented by red points and crossbars. The number of gonads analyzed per condition are represented by *n*, and tests are based on data from 3,933 control cell detections and 8,134 depletion cell detections. A two-tailed Welch's two-sample *t*-test suggests that the average DAPI intensity is significantly different across conditions, though the effect size is minimal (top). Similarly, a one-tailed Welch's two-sample *t*-test suggests that H3K4me3/DAPI intensity is higher on average in depletion gonads, though the magnitude of difference is small (bottom). Relationship between germ cell position on linear gonad axis and H3K4me3/DAPI intensity **(C)** or per-gonad scaled H3K4me3 intensity **(D)**. Each point represents a germ cell detection, based on data from 3,933 control cell detections and 8,134 depletion cell detections from 50 and 77 gonads, respectively.

DISCUSSION

In this study, we investigated non-ribosomal functions of the nucleolus during oogenesis using separation-of-function strains in *Caenorhabditis elegans*. By leveraging the auxin-inducible degron (AID) system, we selectively depleted a catalytic subunit of RNA Polymerase I (Pol I) and a ribosome assembly factor in the germline. This approach enabled us to distinguish between the effects of nucleolar disruption and reduced ribosome biogenesis, revealing that germ cell nucleoli actively regulate meiotic progression through epigenetic mechanisms independent of ribosome production. Our findings uncover a previously unrecognized role for RNA Pol I activity and nucleolar integrity in oogenesis beyond ribosome production.

Differential impacts of nucleolar versus ribosomal stress on oogenesis

A key insight from our work is the distinct impact of nucleolar versus ribosomal stress on germ cell differentiation. Near-complete reduction of ribosome assembly had minimal consequences for oocyte production (**Figure 3**), suggesting that the oogenesis program, including meiotic chromosome restructuring and histone remodeling, is not heavily dependent on ribosome biogenesis (**Figure 4-5**). In contrast, disruption of nucleolar structure through near-complete reduction of RNA Pol I activity leads to significant oogenesis defects (**Figure 3-4**). These results suggest that nucleolar integrity, rather than downstream capacity for protein synthesis, is essential for proper germ cell progression through oogenesis.

Our previous work highlights the importance of ribosome loading in maturing oocytes to support embryogenesis in *C. elegans* [22]. However, our current results show that ribosome biogenesis is not critical for oogenesis itself, at least within the timeframe of our investigation. Furthermore, we previously demonstrated that somatic chromatin reorganization and developmental progression beyond the L2 stage are similarly affected by either nucleolar or ribosomal stress, indicating a uniform response in somatic tissues [43,60]. Here, however, germ cells exhibit a unique sensitivity to nucleolar disruption, suggesting that meiotic cells, with their distinct chromatin remodeling requirements, are particularly vulnerable to changes in nucleolar homeostasis.

One explanation may be that meiotic germ cells, which are relatively quiescent in their transcription and translation activities, do not strongly depend on ongoing ribosome production. However, their reliance on large–scale chromosome restructuring places them at risk when nucleolar integrity is compromised; several lines of evidence in other organisms and tissues suggest that nucleolar integrity is linked to genome organization and stress sensing [61–66]. In female gametogenesis in particular, intact nucleolar structure has been shown to have several implications for successful oogenesis unrelated to ribosome production. These functions include safeguarding genomic stability by shielding repetitive rDNA loci from recombination, preserving satellite repeat sequences, and sequestering transcriptional silencing factors, all of which are crucial for successful oogenesis [23–25]. Thus, given the potential consequences of aberrant nucleolar structure in maturing germ cells, it is likely that nucleolar stress-sensing mechanisms play a role in regulating meiotic progression.

In support of this view, partial reductions in RNA Pol I activity or ribosome assembly, both of which maintain a spherical nucleolar structure, do not impair meiotic progression based on our assessment of transition zone and pachytene chromosome morphology (**Figure 4**). In contrast, near-complete depletion

of RNA Pol I activity, accompanied by nucleolar disruption, results in abnormal meiotic chromosome morphologies and significantly reduced oocyte production (**Figure 3-4**). These findings strongly suggest a nucleolar stress response that directly impairs meiotic progression, independent of any downstream effects on protein synthesis.

Chromatin remodeling drives meiotic defects in response to nucleolar disruption

Although nucleolar disruption clearly impacts chromatin organization, we did not observe a correlation between promoter accessibility and mature mRNA levels (**Figure S3**). This is consistent with another study in *C. elegans* that found no correlation between ATAC-seq signal and active transcription in isolated germ cells [4], suggesting that chromatin accessibility alone does not fully account for gene expression regulation in the germline. Germline mRNA expression may instead be regulated by other mechanisms, including 22G-RNA and piRNA silencing (21U-RNAs) [67–69], inhibition of RNA Polymerase II carboxyl-terminal domain phosphorylation by PIE-1 [70], and post-transcriptional 3'UTR regulation controlled by RNA-binding proteins, such as PUF family proteins or GLD-1 [71–74].

Our data suggest that disruptions in chromatin conformation alone, driven by nucleolar cap formation, are sufficient to impair meiotic progression and reduce oocyte production. Given the extensive chromatin reorganization required in meiotic cells compared to other non-differentiating cell states, it is plausible that germ cells may be particularly vulnerable to such significant disturbances in nuclear architecture, even if these do not immediately affect transcriptional output.

How nucleolar structure might drive meiotic chromatin dynamics

Two potential mechanisms may explain why nucleolar disruption impair meiotic progression, particularly through aberrant chromatin remodeling.

First, the disassembly of nucleolus via near complete depletion of RNA Pol I could release ribosomal proteins or other factors (e.g. MDM2) that, in other organisms, stabilize P53 or similar pathways to trigger cell cycle arrest [75,76]. Although *C. elegans* lacks a direct MDM2 homolog, analogous pathways may be at play to prevent meiotic entry, potentially explaining the observed oogenesis defect.

Second, nucleolar caps may function as stress sensors for DNA damage or incompletely replicated rDNA, activating surveillance pathways that stall meiotic progression. This model is supported by findings in other systems showing that nucleolar stress can prompt G2 arrest through ATR-Chk-1 signaling, independent of ribosome depletion [77]. In *C. elegans*, rDNA loci may become exposed prematurely when nucleolar structure is compromised, leading to activation of ATM/ATR pathways and diverting double-strand break repair or chromatin-modifying complexes toward rDNA repeats. Given that proper ATM and ATR activity is critical for organization of chromosomes along the cohesin axis and normal meiotic progression [78,79], exposure of rDNA loci could disrupt the balance of ATM/ATR activity, leading to prophase arrest in RPOA-2-depleted animals. Since H3K4 methyltransferases can localize to double-strand break sites [80], this stress-driven redistribution of repair machinery might also underlie the misregulated H3K4me3 pattern observed in our study.

Spatiotemporal control of H3K4 methylation by the nucleolus during oogenesis

Our work demonstrates that premature nucleolar disassembly during oogenesis impairs germ cell maturation, primarily through its effects on chromatin remodeling. Specifically, the regulation of H3K4-related chromatin dynamics is critical for oogenesis, as H3K4me3 levels need to gradually increase along the distal-proximal axis to prime the promoters of genes required for zygotic genome activation [4]. Disruptions in the activity of H3K4 de/methylases have been linked to abnormal nuclear morphology, reduced oocyte production, and inability to enter meiosis [11–13]. In agreement, we find that premature nucleolar disruption weakens the H3K4 remodeling gradient, leading to defects in chromatin architecture and oocyte production. This highlights a novel role for nucleolar integrity as a critical upstream regulator of the spatiotemporal regulation of H3K4 methylation necessary for germ cell maturation.

Our gonadal ATAC-seq analyses further reveal that nucleolar disruption uniquely increases chromatin accessibility at oogenesis genes, oogenesis-promoting EFL-1-binding sites, and promoters undergoing H3K4me3 remodeling during oogenesis. We propose a model in which germ cells experiencing nucleolar stress redirect H3K4 methyltransferases or other remodeling factors to the site of rDNA damage, thereby depleting them from normal chromatin remodeling tasks. This shift may lead to hyper-accessible yet transcriptionally inactive loci in the germline, consistent with the disruption of the normal H3K4me3 gradient and oogenesis-related gene priming.

Furthermore, our single-cell analysis of H3K4me3 immunofluorescence reveals that the positive H3K4me3 gradient along the distal-proximal gonad axis is disrupted under nucleolar stress. This perturbation is mediated by premature deposition of H3K4me3 in the distal region, further supporting the misregulation of chromatin accessibility in oogenesis genes. However, without single-cell ATAC-seq resolution, it remains unclear how chromatin accessibility changes are distributed along the gonad axis.

Although H3K4me3 represents a major dynamic mark in oocyte development, H3K27 methylation is also critical for germline maintenance, and these marks are generally mutually exclusive [4]. It remains possible that misregulated heterochromatin marks, such as H3K27me3, contribute to the nucleolar-disruption phenotype. Intriguingly, H3K27 methylation has been associated with the nucleolus in other contexts [62], further hinting that a global shift in histone marks underlies the oogenesis defects we observed.

Broad implications

While our study focuses on *C. elegans*, nucleolar integrity and H3K4me3 remodeling during oogenesis are evolutionary conserved in higher eukaryotes, including humans [5–10]. This suggests that nucleolus may play a similarly critical, non-ribosomal role in female gametogenesis in other species. The sensitivity of meiotic germ cells to nucleolar stress has significant implications for reproductive health [81], particularly in individuals exposed to environmental stress, undergoing aging, or affected by ribosomopathies.

Our findings also highlight potential explanations for phenotypic differences observed in disorders linked to Pol I components, such as Treacher Collins syndrome, which involves mutations in *POLR1B*, and uniquely impacts neural crest proliferation and migration [82,83]. By uncovering how nucleolar driven chromatin reorganization shapes germ cell maturation, we provide a conceptual framework for

696 understanding how disruptions in rDNA transcription can lead to specialized developmental deficits. More
697 broadly, understanding these nucleolar roles offers a window into the intersection of genome maintenance,
698 chromatin remodeling, and cell fate decisions across Metazoan development.

699 **ACKNOWLEDGEMENTS**

700 We thank Trevor F. Freeman for generating ATAC-seq libraries. We thank Ayush Desai and Ajay Panda
701 for their assistance with imaging experiments and vector construction used in this study, respectively. We
702 thank Sarinay Cenik lab members, Cenik lab members, Can Cenik, Arlen Johnson, Steve Vokes, and Keiko
703 Torii for constructive criticism and discussions.

704 This work was supported by the UT CNS Catalyst Grant, National Institutes of Health (NIH) NIGMS
705 (R35GM138340), and Welch Foundation (F-2133-20230405) grants to E.S.C. Some strains were provided
706 by the CGC, which is funded by NIH Office of Research Infrastructure Programs (P40 OD010440).

707 **AUTHOR CONTRIBUTIONS**

708 R.M.T. and E.S.C. conceptualized the project and co-wrote the original manuscript. R.M.T. designed and
709 conducted all experiments, performed all formal analysis, and generated all visualizations. Q.Z. generated
710 strains and provided suggestions for experimental design. A.R. generated the ATAC-seq and RNA-seq
711 libraries. E.S.C. supervised the project and acquired funding.

712 **RESOURCE AVAILABILITY**

713 **Lead contact**

714 Requests for further information and resources should be directed to and will be fulfilled by the lead contact,
715 Elif Sarinay Cenik (esarinay@utexas.edu).

716 **Data availability**

717 ATAC-seq and RNA-seq libraries are available through NCBI GEO, with accession codes GSE290498 and
718 GSE290499, respectively. Data will be publicly released upon successful review of this article.

719 **Code availability**

720 Original pipeline used for germ nuclei linearization and confocal intensity quantification is hosted on the
721 GitHub repository: https://github.com/raqmejtru/germ-nuclei-linearization. Code will be publicly released
722 upon successful review of this article.

723 **DECLARATION OF INTERESTS**

724 The authors declare no competing interests.

METHODS

Strain generation

Constructs and strains used in this study are listed in **Table S7**-**S8**, respectively.

The *mKate2* tagged *nucl-1* allele was constructed using Cas9 protein driven by *eft-3* promoter in pDD162 and gRNA targeting a genomic sequence in the C-terminus of *nucl-1* in pAR2, a derivative of pRB1017, an empty vector for gRNA cloning. The sgRNA construct pAR2 was generated by the oligos ESC-AR-5 and ESC-AR-6. *nucl-1::mkate2::c1^sec^3xflag* (pAR1) was constructed for generating the knock-in into the C-terminus of the *nucl-1* gene. The 5′ and 3′ homology arms were amplified ~500 bp upstream of *nucl-1* stop codon using oligos ESC-AR-7 and ESC-AR-8, and ~500 bp downstream of stop codon using ESC-AKP-40 and ESC-AKP-41. The repair templates were used to replace the ccdB in pDD285.

Oligos ESC-AKP-(7-8) were used to generate a sgRNA targeting the N-terminus of the *dao-5* gene (16 bp from start codon) in pAKP2. The 5' homologous arm (500 bp upstream of *dao-5* start codon) and 3' homologous arm (500 bp downstream of start codon) were amplified using oligos ESC-AKP-(1-4), and subsequently used to replace the ccdB cassette in pDD282 to construct the repair template plasmid pAKP1.

All plasmids for microinjection were purified using the PureLink HiPure Plasmid Miniprep Kit (Invitrogen #K210002). Oligo sequences used to generate these plasmids are in **Table S6**.

Strains generated through microinjection were prepared according to guidelines from Dickinson et al., 2015. To generate ESC254, N2 animals were injected with a mix consisting of 50 ng/µL pDD162, 50 ng/µL gRNA pAKP2, 50 ng/µL *dao-5* repair template of pAKP1, and 5 ng/µL of pCFJ104 as an extrachromosomal marker. The SEC was then excised by heat shock. To generate ESC770, N2 animals were injected with a mix consisting of 50 ng/µL pDD162, 50 ng/µL gRNA pAR2, 50 ng/µL *nucl-1* repair template of pAR1, and 5 ng/µL extrachromosomal marker L3785. Animals lacking the extrachromosomal array were heat-shocked to remove the SEC. To generate ESC772, DLW109 animals were injected with a mix consisting of 50 ng/µL pDD162 (Cas9 vector), 50 ng/µL gRNA pRR13, 50 ng/µL *rpoa-2* repair template of pQZ43, and 5 ng/µL extrachromosomal marker pCFJ104. Finally, animals without the extrachromosomal array were heat-shocked to excise the SEC.

To visualize nucleolar structure while depleting RPOA-2 or GRWD-1, we crossed the *nucl-1::mKate2* reporter (ESC770) into the RPOA-2 AID background (ESC772) and GRWD-1 AID background (ESC796) to produce ESC794 and ESC797.

Lastly, to examine the co-localization of nucleolar structure and chromatin during meiosis, we crossed the *nucl-1::mKate2* reporter (ESC770) into a background containing a reporter for the synaptonemal complex (CA1218).

Worm growth

C. elegans strains were maintained on plates with agar and nematode growth media (NGM) that were seeded with *Escherichia coli* strain OP-50. Animals were grown at 20°C for all experiments. Prior to experiments, animals were synchronized either by bleach synchronization or by allowing adults to lay

embryos for two hours. The synchronized embryos were grown on NGM agar plates until they reached the late L4 stage. At the late L4 stage, animals were transferred to control or auxin treatment plates for further analysis.

Auxin treatment

To deplete our proteins of interest using the auxin-inducible degron system (AID) system, we used a natural auxin (IAA) compound from Alfa Aesar (#A10556). A 400 mM stock solution was prepared in EtOH and stored at −20°C. For auxin treatment plates, we diluted IAA to a 1 mM concentration in NGM agar, then poured and let it solidify in plates. For control treatment plates, we diluted an equivalent volume of ethanol into NGM agar, then also poured and let it solidify in plates. Once solidified, plates were seeded with OP-50 and set to incubate at 20°C overnight to allow lawn growth. Synchronized late L4 worms were then transferred onto control or auxin plates for 18 hours at 20°C. Prior to any subsequent experiments, a qualitative assessment of GFP depletion was performed on a fluorescent dissection scope to ensure that auxin treatment worked as expected.

Confocal imaging

Two-dimensional and 3-D confocal images were captured using a STELLARIS 8 microscope (Leica Microsystems). For 3-D images, Z-stacks were either transformed into an average projection or rendered in 3-D using LAS-X software (Leica Microsystems). For images that are presented for qualitative purposes, we adjusted the brightness and contrast to highlight features of interest, ensuring that adjustments are identical across treatments/conditions. Images used for statistical quantification were analyzed in their raw form without adjustments.

Quantification of GFP signal

Imaging slides were prepared by transferring worms onto an immobilizing solution (10 mM levamisole hydrochloride, Sigma-Aldrich #31742-250MG). Gonads were dissected by using a hypodermic needle to slice near the head region. GFP signal was captured using a 10X objective with a GFP filter on a Leica STELLARIS 8 microscope with consistent intensity and exposure settings (Leica Microsystems).

For **Figure S1A**, after imaging, CellProfiler v4.2.6 was used to segment individual nuclei and measure signal intensity based on the average signal of each segmented nucleus [85]. Statistical comparison of mean GFP intensity between control and auxin treatments was carried out using a one-tailed Welch two-sample *t*-test, performed with the `t.test` function in R [86].

For **Figure 4A**, after imaging, QuPath v0.5.1 was used to manually annotate gonads using morphology from the bright-field channel, and these annotations were copied onto the GFP channel [87]. Mean intensities were measured within gonad annotations for downstream analysis using default parameters. To provide a relative measure of the amount of RPOA-2 depletion at various concentrations of auxin, mean degron::GFP::RPOA-2 intensities were scaled with 0 μM treated maximum set to 1, and 1000 μM treated minimum set to 0.

Quantification of apoptotic corpses

Acridine orange (AO) staining was used to count apoptotic corpses in young adult germlines. First, L4s were transferred onto control or 1 mM IAA plates seeded with OP50 for 16 hours. We confirmed that the degron::GFP::RPOA-2 signal was visibly reduced in the auxin-treated animals under a fluorescent dissection scope prior to continuing with AO staining. After 16 hours, each plate was spiked with 500 µL of AO stain, which was prepared using 2 µL of 10 mg/mL AO (Invitrogen™ #A1301) dissolved in 1 mL of M9 buffer. Animals were left to feed on the stain for one hour, and were subsequently transferred onto new control or 1 mM IAA plates to de-stain for an additional hour before live imaging in levamisole.

Fluorescent microscopy was used to identify strong GFP signals characteristic of apoptotic corpses that retain a green AO signal. We counted the number of corpses per one gonad arm per animal, and used a Mann-Whitney *U*-test to compare the distribution of corpses across control and auxin-treated samples. Lastly, we co-examined NUCL-1::mKate2 localization to confirm that degron::GFP::RPOA-2 was depleted, since the green AO signal obscures the GFP-tagged protein.

Quantification of germline morphology

After control or auxin treatment, animals were transferred to slides with an immobilizing agent (10 mM levamisole hydrochloride, Sigma-Aldrich #31742-250MG). We captured whole-worm images for body measurements using a 10X DIC objective and germline morphology images using a 63X DIC objective on a STELLARIS 8 microscope (Leica Microsystems). Using ImageJ, we measured body area, the length of the proximal arm (from the edge of the "-1" oocyte to the edge of the U-shaped arm bend), and the length and area of the three most proximal oocytes based on eggshell boundaries [88]. Oocyte counts were measured by scanning vertical stacks for nuclear and eggshell boundaries while imaging. Statistical comparisons were performed with the `t.test` function in R [86].

SPY555-DNA probing

Following control or auxin treatment, animals were transferred to slides with 4.5 µL of 10 mM levamisole hydrochloride (Sigma-Aldrich #31742-250MG). Gonads were dissected by using a hypodermic needle to slice near the head region. Next, 0.5 µL of 1000X SPY555-DNA eluted in DMSO (Cytoskeleton #CY-SC201) was added to the dissected animals and left to incubate for approximately 30 minutes.

We captured SPY555-DNA fluorescence in dissected gonads using confocal Z-stacks of identical resolutions that encompassed as many zones as possible through approximately half of the sheath to mid slice of the syncytium.

Library preparation

After control or auxin treatment, worms were transferred onto a slide with an immobilizing solution (1 mM levamisole hydrochloride, Sigma-Aldrich #31742-250MG). Gonads were dissected by using a hypodermic needle to slice near the head region. Twenty dissected gonads were collected per replicate into ddH_2O.

For RNA-seq, the dissected gonads were transferred to 1 mL of TRIzol (Thermo Fisher Scientific), vortexed, then incubated for 5 minutes at room temperature. RNA was extracted by adding 200 µL of chloroform to the lysate, spinning for 10 minutes at 15,000 rpm, and isolating the supernatant. The isolated RNA was precipitated overnight at −20°C using 50 mM sodium acetate, 5 mM $MgCl_2$, 15 mg/mL GlycoBlue™ Coprecipitant (Thermo Fisher Scientific #AM9515), and isopropanol. RNA pellets were washed in 80% ethanol and prepared using the SMARTer Stranded RNA-Seq kit (Takara #634839). Briefly, the libraries were prepared by fragmenting and converting RNA to cDNA, and PCR amplified. PCR amplification reactions were run as follows: 1 minute denaturation at 94°C, followed by 15-17 cycles with 15 seconds at 98°C, 15 seconds at 55°C, and 30 seconds at 68°C. After PCR amplification, the DNA libraries were further purified using Agencourt AMPure XP beads (Fisher Scientific #A63880). The resulting libraries were quantified using the Qubit™ dsDNA HS Assay Kit (Thermo Fisher Scientific #Q32851) and sequenced on a NovaSeq 6000 v1.5 SP flow cell (Illumina).

For ATAC-seq, the dissected gonads were stained with DAPI (5 ng/µL in PBS), then loaded onto a hemocytometer for nuclei counting. A volume containing 50,000 nuclei was then mixed with 2.5 µL TDE1 tagmentase. The tagmentation reaction was incubated at 37 °C for 30 minutes on a shaker. Immediately after, the reactions were cleaned using the Zymo DNA Clean & Concentrator-5 kit (Fisher #NC9674845). The cleaned and tagmented DNA was then amplified with Nextera i5 and i7 adapters using the NEBNext® High-Fidelity 2X PCR Master Mix (NEB M0541L). Amplification reactions were run as follows: 5 minute extension at 72°C; 30 second denaturing at 98°C; 18-19 cycles with 10 seconds at 98°C, 30 seconds at 63°C, and 1 minute at 72°C; and a final extension of 10 minutes at 72°C. PCR products were cleaned to remove adapter contamination using the Zymo DNA Clean & Concentrator-5 kit. Library quality was assessed by checking nucleosome banding patterns on a gel, and passing libraries were subsequently cleaned using Agencourt AMPure XP beads. The resulting libraries were quantified using the Qubit™ dsDNA HS Assay Kit and sequenced on a NovaSeq 6000 v1.5 SP flow cell (Illumina).

Quantification of rDNA transcription

Raw RNA-seq reads were trimmed with Trim Galore! v0.6.10 using default parameters [89]. HISAT2 v2.2.1 was then used to build an index of the WBcel235 genome using the command `hisat2-build --seed 40` [90]. To report all multimapping alignments to repetitive rDNA regions, reads were mapped using the command `hisat2 --seed 40 --all`. Alignments were coordinate sorted using Picard SortSam v3.1.1 with the command `-SORT_ORDER coordinate --CREATE_INDEX true` [91].

To quantify rDNA transcription, we manually curated “gene” annotations for the two unique internal transcribed spacers (ITS) and appended them to the WBcel235 annotation. We assessed alignment counts to the modified annotation using featureCounts v2.0.6 with parameters `-t gene -g gene_id -M -O --fraction -p` [92]. A Welch two-sample *t*-test was performed to compare mean counts per million reads mapped to each ITS region as well as the entire 45S region using the `t.test` function in R [86].

For a visual comparison of coverage in the rDNA region, we used bamCoverage v3.5.4 to normalize reads to average counts per million using the parameters `--normalizeUsing CPM --binSize 25` [93]. Coverage was later visualized in R using the Gviz v1.47.1 package [94].

868 **Identification of differentially expressed genes**

869 Raw RNA-seq reads were trimmed with Trim Galore! v0.6.10 using default parameters [89]. HISAT2 v2.2.1
870 was then used to build an index of the WBcel235 genome using the command `hisat2-build --seed 40` [90].
871 Reads were mapped using the command `hisat2 --seed 40` with default parameters. Alignments were
872 coordinate sorted using Picard SortSam v3.1.1 with the command `-SORT_ORDER coordinate --
873 CREATE_INDEX true` [91]. Alignment counts were then summarized using featureCounts v2.0.6 with
874 parameters `-t exon -g gene_id -p` [92]. Before further analyses, we filtered genes down to the 19,985 protein
875 coding genes found in the WBcel235 annotation, and we also filtered out genes with low expression (less
876 than 5 counts across 3 biological replicates). We evaluated differential gene expression using DESeq2
877 v1.40.2 with an experimental design that accounted for strain and treatment [95]. Genes were considered
878 differentially expressed if they had a Benjamini-Hochberg adjusted *p*-value < 0.05.

879 **Identification of differentially accessible regions**

880 Raw ATAC-Seq reads were trimmed, aligned, decontaminated, and quality assessed using the SRAtac
881 v0.5.0 pipeline [60]. Before performing differential accessibility analyses, we used RUVSeq v1.34.0 to
882 perform batch correction on mapped counts by computing estimated factors of unwanted variance against
883 an empirical set of control genes [96]. We arbitrarily selected control genes with *p*-values greater than 0.75
884 and an average count per million above 20 in at least 90% of samples, calculated with the `filterByExpr`
885 function in edgeR v3.42.4 [97].

886 To evaluate differentially accessible chromatin regions (DARs), we used DESeq2 v1.40.2 with an
887 experimental design that accounted for strain, treatment, and the estimated factors of unwanted variation [95].
888 We compared DARs across non-depleted and depleted samples using a significance threshold of a
889 Benjamini-Hochberg adjusted *p*-value < 0.05. To visualize DARs, we performed $\log_2$ fold-change
890 shrinkage using DESeq2's `lfcShrink` function with apeglm v1.22.1 shrinkage estimators [98].

891 **ATAC-seq genomic feature annotation**

892 ATAC-seq peaks were annotated using the `annotatePeak` function in the ChIPseeker v1.36.0 package with
893 modification `overlap = all` [99] in conjunction with the TxDb ce11 v3.4.6 reference database [100]. Results
894 were visualized with the `plotAnnoBar` function in the clusterProfiler v4.12.0 package [101,102].

895 **Differential analysis of functional gene ontology (GO) biological processes**

896 For both ATAC-seq and RNA-seq, differential analysis of functional gene ontology (GO) biological
897 processes were performed using the `compareCluster` function in the clusterProfiler v4.12.0 package using
898 the following parameters: fun = 'enrichGO', ont = 'BP', pAdjustMethod = 'fdr', pvalueCutoff = 0.0001
899 (ATAC) or 0.001 (RNA), qvalueCutoff = 0.0001 (ATAC) or 0.001 (RNA) [101,102]. Results were visualized
900 using the `dotplot` function in the enrichplot v1.24.0 package using parameter showCategory = 3 [103].

901 **Motif enrichment and characterization**

902 The MEME-suite bed2fasta tool was used to add nucleic sequences to background and differentially
903 accessible peaks based on the UCSC ce11 reference genome [104]. We used the MEME-suite STREME tool

to enrich for ungapped motifs present in our peak sets with a *p*-value and *E*-value threshold of 0.05, an alignment around the center of the peak, and all other default parameters [105]. We used the MEME-suite Tomtom tool [106] to map the enriched motifs against the 842 TF motifs present in the TFBSshape database [53]. We classified significant motif-motif similarity based on Pearson correlation coefficients, an *E*-value threshold of 8.42, and all other default parameters. We further manually curated matches to combine redundant query motifs and their repeated hits, and ensure that alignments were visibly cohesive.

To identify genomic sites in our ATAC-seq data containing the *C. elegans* EFL-1 motif (MA0541.1), we used the MEME-suite FIMO v5.5.5 tool with parameters `--thresh 1.0E-4 --nrdb--` against our background set of peaks (i.e., all peaks across all samples called in SRAtac pipeline). We identified which peaks contained EFL-1 motifs by searching for overlaps between EFL-1 motif sites and peaks using the `findOverlaps` function with parameter `type = ‘within’` in the GenomicRanges v1.56.1 package [107]. Genes with EFL-1 motifs in their promoter were analyzed for enrichment of GO biological processes using the enrichGO function in the in the clusterProfiler v4.12.0 package with parameters `pAdjustMethod = 'fdr', pvalueCutoff = 0.05, qvalueCutoff = 0.05` based on the annotation of the peak that the motif was located in [101,102]. Results were visualized using the `dotplot` function in the enrichplot v1.24.0 package using parameter showCategory = 3 [103].

Metagene analysis of histone ChIP-seq coverage

Isolated germ and oocyte histone ChIP-seq experiments used in this study are listed in **Table S9**.

Raw ChIP-seq reads were downloaded from NCBI using the SRA Toolkit [108]. Reads were processed using the nf-core/chipseq pipeline with parameters: `--genome WBcel235 --broad_cutoff 0.01 --macs_fdr 0.001 --nomodel` and `--extsize` between 147-250 [109,110]. If read length was known, we specified the `--read_length` parameter, otherwise we specified the effective genome size (`--macs_gsize 100286401`) estimated using the recommended `faCount` tool [111].

Next, bigwigAverage v3.5.5 was used to compute an average bigwig coverage track for each antigen and cell type combination (i.e., oocyte H3K4me3 antigen, oocyte H3K4me3 input, etc.) using parameter `--scaleFactors` with the scale factors provided by the nf-core/chipseq pipeline [93]. Average $\log_2$ ratios of coverage across antigen/input samples were then computed using bigwigCompare v3.5.5 with parameter `--operation log2` [93]. Additionally, an average $\log_2$ coverage score was computed across significantly more accessible peaks after RPOA-2 depletion and an identically-sized random subset of ATAC-seq peaks by intersecting bigwig scores using the `findOverlaps` function in the GenomicRanges v1.56.1 [107].

Metagene profile plots were used to display the average $\log_2$ ratios of ChIP signal from isolated germ cells or oocytes across peaks that were significantly more accessible after RPOA-2 depletion, or across an identically-sized random subset of promoter ATAC-seq peaks that were not significantly more accessible. The tool computeMatrix v3.5.5 was used to generate coverage scores per peak using parameters `--referencePoint center --afterRegionStartLength 1000 --beforeRegionStartLength 1000 --binSize 25` [93]. Metagene plots were displayed using plotProfile v3.5.5 with parameter `--perGroup` to summarize scores across germ versus oocyte cell types [93].

Analysis of chromatin accessibility across H3K4me3-remodeled gene clusters

Scaling (size) factors for ATAC-seq peak counts were computed using the relative log expression (RLE) normalization method from DESeq2 v1.40.2 [95]. Each sample's ATAC-seq coverage was re-scaled and binned into bigwigs for downstream visualization using bamCompare v3.5.5 with parameters `--scaleFactor (1/RLE size factor) --binSize 50` [93]. RLE-normalized coverage for depletion and control samples was aggregated using bigwigAverage v3.5.5, and subsequently $\log_2$ transformed using bigwigCompare v3.5.5 `--operation log2` to interpret fold changes in coverage across depletion and control conditions [93].

Metagene profile plots were used to display the average $\log_2$ ratios of ATAC signal across the H3K4me3-remodeled gene clusters. The tool computeMatrix v3.5.5 was used to generate coverage scores per gene using parameters `scale-regions --afterRegionStartLength 1000 --beforeRegionStartLength 1000 --regionBodyLength 1000 --binSize 25` [93]. Metagene plots were displayed using plotProfile v3.5.5 with parameter `--perGroup` to summarize scores across cluster 1, 2, and 3 gene sets [93].

H3K4me3 immunostaining and signal quantification

Prior to immunostaining, we confirmed that the degron::GFP::RPOA-2 signal was visibly reduced in the auxin-treated animals using a GFP filter on a Leica STELLARIS 8 microscope (Leica Microsystems).

H3K4me3 immunostaining was performed on tube-fixed dissected gonads from adult worms after control or auxin treatment. Briefly, gonads were dissected in a solution with levamisole and 0.05% Tween 20 in PBS (PBS-T). Dissected bodies were transferred to DNA LoBind™ Tubes (Eppendorf™ #022431021) and fixed for five minutes using 4% PFA, then washed three times with PBS-T. Next, gonads were permeabilized for fifteen minutes using 0.5% Triton X-100 in PBS-T. Gonads were then post-fixed using 95% ethanol for five minutes at -20°C, washed three times in PBS-T, and blocked for one hour using 5% BSA in PBS-T. For primary antibody incubation, half of the gonads from each treatment condition were incubated overnight at 4°C in 2% BSA in PBS-T as a negative primary antibody control, while the other half were incubated overnight at 4°C using a 250X dilution of Rabbit Anti-Histone H3 (tri-methyl K4) antibody (Abcam #ab8580) in 2% BSA in PBS-T. Gonads were subsequently washed three times using PBS-T and incubated at room temperature for two hours in 10 µg/mL of Goat Anti-Rabbit IgG (H+L) Cross-Absorbed Alexa Fluor™ 633 secondary antibody (Invitrogen™ #A-21070) in 2% BSA in PBS-T. Finally, gonads were washed three times with PBS-T and mounted onto slides using VECTASHIELD® Antifade Mounting Medium with DAPI (1.5 µg/mL) (Vector Laboratories #H120010).

Immunostained gonads were imaged from the distal to proximal zones using 40X tile-scanned confocal Z-stacks of identical resolutions (2048x2048). All Z-stacks were forced to encompass 3 µm to minimize overlaps between nuclei for downstream nuclei segmentation. Additionally, all confocal images were captured using identical laser intensity and gain settings for downstream intensity quantification. We excluded imaging gonads that were not adequately laying flat on the slide, preventing us from completely capturing the distal to proximal zones within a 3 µm vertical space. Lastly, Z-stacks were transformed into average projections for further analyses using LAS-X software (Leica Microsystems).

A custom QuPath v0.5.1 script was created to identify H3K4me3 signal intensity per nuclei following RPOA-2 control or depletion treatment. Briefly, gonads were manually annotated based on morphology

from the T-PMT confocal channel, and these annotations were overlaid onto the corresponding DAPI channel. Gonad annotations were segmented using the `StarDist2D` function on the DAPI channel with the `dsb2018_heavy_augment.pb` model and parameters `normalizePercentiles(1, 99)`, `threshold(0.80)`, `pixelSize(0.1)`, and `cellExpansion(0)` [87,112]. Segmented nuclei annotations were copied to the H3K4me3 channel. Average H3K4me3 and DAPI signal intensities within segmented nuclei were measured using the `addIntensityMeasurements` function with parameter `downsample = 0.1`. We converted average signal intensity to integrated signal intensity using the formula `integrated intensity = mean intensity * area of detected nuclei` to prevent nuclei detection area from biasing intensity comparisons across differently sized nuclei. Additionally, to account for differences in permeability across gonads during immunostaining (due to varying physical damage while vortexing, etc.), we normalized integrated H3K4me3 intensity to integrated DAPI signal, and separately to the maximum H3K4me3 intensity recorded per gonad (**Figure S4B-D**).

To analyze variation in H3K4me3 intensity from the distal to proximal zones, we employed a variation of a gonad linearization algorithm to track the location of each nuclei along a linearized gonad representation [113]. Briefly, in QuPath, a polyline skeleton was drawn from the distal tip to the most proximal end of the gonad. We computed perpendicular projections of each nuclei onto the nearest gonad skeleton segment and used this value to calculate the position of each nuclei along the gonad skeleton (see **Figure S4A** and **Figure 6F** for visualizations). We limited our analyses to nuclei that were within a linearized gonad length of 2,000 px.

Lastly, for each gonad, we evaluated the positive non-parametric correlation between nuclei position along the linear gonad axis and integrated H3K4me3/DAPI intensity or per-gonad scaled H3K4me3 intensity using the `cor.test` function in R with parameters `method='spearman', alternative='greater', exact='false'` and corrected for false positives using the `p.adjust` function in R with parameter `method='BH'`.

REFERENCES

1. Hamatani T, Carter MG, Sharov AA, Ko MSH. Dynamics of Global Gene Expression Changes during Mouse Preimplantation Development. *Dev Cell*. 2004;6(1):117-131. doi:10.1016/S1534-5807(03)00373-3
2. Vastenhouw NL, Cao WX, Lipshitz HD. The maternal-to-zygotic transition revisited. *Development*. 2019;146(11):dev161471. doi:10.1242/dev.161471
3. Tadros W, Lipshitz HD. The maternal-to-zygotic transition: a play in two acts. *Development*. 2009;136(18):3033-3042. doi:10.1242/dev.033183
4. Mazzetto M, Gonzalez LE, Sanchez N, Reinke V. Characterization of the distribution and dynamics of chromatin states in the C. elegans germline reveals substantial H3K4me3 remodeling during oogenesis. *Genome Res*. Published online December 26, 2023. doi:10.1101/gr.278247.123
5. Blythe SA, Cha SW, Tadjuidje E, Heasman J, Klein PS. β-catenin Primes Organizer Gene Expression By Recruiting a Histone H3 Arginine 8 Methyltransferase, Prmt2. *Dev Cell*. 2010;19(2):220-231. doi:10.1016/j.devcel.2010.07.007
6. Vastenhouw NL, Zhang Y, Woods IG, et al. Chromatin signature of embryonic pluripotency is established during genome activation. *Nature*. 2010;464(7290):922-926. doi:10.1038/nature08866
7. Zhang Y, Vastenhouw NL, Feng J, et al. Canonical nucleosome organization at promoters forms during genome activation. *Genome Res*. 2014;24(2):260-266. doi:10.1101/gr.157750.113
8. Dahl JA, Jung I, Aanes H, et al. Broad histone H3K4me3 domains in mouse oocytes modulate maternal-to-zygotic transition. *Nature*. 2016;537(7621):548-552. doi:10.1038/nature19360
9. Zhang B, Zheng H, Huang B, et al. Allelic reprogramming of the histone modification H3K4me3 in early mammalian development. *Nature*. 2016;537(7621):553-557. doi:10.1038/nature19361
10. Xia W, Xu J, Yu G, et al. Resetting histone modifications during human parental-to-zygotic transition. *Science*. 2019;365(6451):353-360. doi:10.1126/science.aaw5118
11. Laranjeira AC, Berger S, Kohlbrenner T, Greter NR, Hajnal A. Nutritional vitamin B12 regulates RAS/MAPK-mediated cell fate decisions through one-carbon metabolism. *Nat Commun*. 2024;15(1):8178. doi:10.1038/s41467-024-52556-3
12. Xiao Y, Bedet C, Robert VJP, et al. Caenorhabditis elegans chromatin-associated proteins SET-2 and ASH-2 are differentially required for histone H3 Lys 4 methylation in embryos and adult germ cells. *Proc Natl Acad Sci*. 2011;108(20):8305-8310. doi:10.1073/pnas.1019290108
13. Käser-Pébernard S, Müller F, Wicky C. LET-418/Mi2 and SPR-5/LSD1 Cooperatively Prevent Somatic Reprogramming of C. elegans Germline Stem Cells. *Stem Cell Rep*. 2014;2(4):547-559. doi:10.1016/j.stemcr.2014.02.007
14. Dubois ML, Boisvert FM. The Nucleolus: Structure and Function. In: Bazett-Jones DP, Dellaire G, eds. *The Functional Nucleus*. Springer International Publishing; 2016:29-49. doi:10.1007/978-3-319-38882-3_2
15. Korčeková D, Gombitová A, Raška I, Cmarko D, Lanctôt C. Nucleologenesis in the Caenorhabditis elegans Embryo. *PLOS ONE*. 2012;7(7):e40290. doi:10.1371/journal.pone.0040290
16. Bjerregaard B, Maddox-Hyttel P. Regulation of ribosomal RNA gene expression in porcine oocytes. *Anim Reprod Sci*. 2004;82-83:605-616. doi:10.1016/j.anireprosci.2004.04.023
17. Fuchs J, Loidl J. Behaviour of nucleolus organizing regions (NORs) and nucleoli during mitotic and meiotic divisions in budding yeast. *Chromosome Res*. 2004;12(5):427-438.

doi:10.1023/B:CHRO.0000034726.05374.db

18. Fulka H, Rychtarova J, Loi P. The nucleolus-like and precursor bodies of mammalian oocytes and embryos and their possible role in post-fertilization centromere remodelling. *Biochem Soc Trans*. 2020;48(2):581-593. doi:10.1042/BST20190847
19. Kresoja-Rakic J, Santoro R. Nucleolus and rRNA Gene Chromatin in Early Embryo Development. *Trends Genet*. 2019;35(11):868-879. doi:10.1016/j.tig.2019.06.005
20. Zatsepina OV, Bouniol-Baly C, Amirand C, Debey P. Functional and Molecular Reorganization of the Nucleolar Apparatus in Maturing Mouse Oocytes. *Dev Biol*. 2000;223(2):354-370. doi:10.1006/dbio.2000.9762
21. Xu D, Chen X, Kuang Y, et al. rRNA intermediates coordinate the formation of nucleolar vacuoles in C. elegans. *Cell Rep*. 2023;42(8). doi:10.1016/j.celrep.2023.112915
22. Cenik ES, Meng X, Tang NH, et al. Maternal Ribosomes Are Sufficient for Tissue Diversification during Embryonic Development in C. elegans. *Dev Cell*. 2019;48(6):811-826.e6. doi:10.1016/j.devcel.2019.01.019
23. Sims J, Copenhaver GP, Schlögelhofer P. Meiotic DNA Repair in the Nucleolus Employs a Nonhomologous End-Joining Mechanism. *Plant Cell*. 2019;31(9):2259-2275. doi:10.1105/tpc.19.00367
24. Fulka H, Langerova A. The maternal nucleolus plays a key role in centromere satellite maintenance during the oocyte to embryo transition. *Development*. 2014;141(8):1694-1704. doi:10.1242/dev.105940
25. Belew MD, Chien E, Michael WM. Characterization of factors that underlie transcriptional silencing in C. elegans oocytes. *PLOS Genet*. 2023;19(7):e1010831. doi:10.1371/journal.pgen.1010831
26. Turowski TW, Tollervey D. Cotranscriptional events in eukaryotic ribosome synthesis. *WIREs RNA*. 2015;6(1):129-139. doi:10.1002/wrna.1263
27. Dash S, Lamb MC, Lange JJ, et al. rRNA transcription is integral to phase separation and maintenance of nucleolar structure. *PLOS Genet*. 2023;19(8):e1010854. doi:10.1371/journal.pgen.1010854
28. Lafontaine DLJ, Riback JA, Bascetin R, Brangwynne CP. The nucleolus as a multiphase liquid condensate. *Nat Rev Mol Cell Biol*. 2021;22(3):165-182. doi:10.1038/s41580-020-0272-6
29. Mukherjee S, Firpo EJ, Wang Y, Roberts JM. Separation of telomerase functions by reverse genetics. *Proc Natl Acad Sci*. 2011;108(50):E1363-E1371. doi:10.1073/pnas.1112414108
30. Son MY, Belan O, Spirek M, et al. RAD51 separation of function mutation disables replication fork maintenance but preserves DSB repair. *iScience*. 2024;27(4). doi:10.1016/j.isci.2024.109524
31. Taddei A, Hediger F, Neumann FR, Bauer C, Gasser SM. Separation of silencing from perinuclear anchoring functions in yeast Ku80, Sir4 and Esc1 proteins. *EMBO J*. 2004;23(6):1301-1312. doi:10.1038/sj.emboj.7600144
32. Ginisty H, Amalric F, Bouvet P. Nucleolin functions in the first step of ribosomal RNA processing. *EMBO J*. 1998;17(5):1476-1486. doi:10.1093/emboj/17.5.1476
33. Roger B, Moisand A, Amalric F, Bouvet P. Nucleolin provides a link between RNA polymerase I transcription and pre-ribosome assembly. *Chromosoma*. 2003;111(6):399-407. doi:10.1007/s00412-002-0221-5
34. Spaulding EL, Feidler AM, Cook LA, Updike DL. RG/RGG repeats in the C. elegans homologs of

Nucleolin and GAR1 contribute to sub-nucleolar phase separation. *Nat Commun*. 2022;13(1):6585. doi:10.1038/s41467-022-34225-5

35. Lee CC, Tsai YT, Kao CW, et al. Mutation of a Nopp140 gene dao-5 alters rDNA transcription and increases germ cell apoptosis in C. elegans. *Cell Death Dis*. 2014;5(4):e1158-e1158. doi:10.1038/cddis.2014.114
36. Rog O, Dernburg AF. Direct Visualization Reveals Kinetics of Meiotic Chromosome Synapsis. *Cell Rep*. 2015;10(10):1639-1645. doi:10.1016/j.celrep.2015.02.032
37. Smolikov S, Eizinger A, Schild-Prufert K, et al. SYP-3 Restricts Synaptonemal Complex Assembly to Bridge Paired Chromosome Axes During Meiosis in Caenorhabditis elegans. *Genetics*. 2007;176(4):2015-2025. doi:10.1534/genetics.107.072413
38. Eberhard R, Stergiou L, Hofmann ER, et al. Ribosome Synthesis and MAPK Activity Modulate Ionizing Radiation-Induced Germ Cell Apoptosis in Caenorhabditis elegans. *PLOS Genet*. 2013;9(11):e1003943. doi:10.1371/journal.pgen.1003943
39. McCarter J, Bartlett B, Dang T, Schedl T. On the Control of Oocyte Meiotic Maturation and Ovulation in*Caenorhabditis elegans*. *Dev Biol*. 1999;205(1):111-128. doi:10.1006/dbio.1998.9109
40. Berry J, Weber SC, Vaidya N, Haataja M, Brangwynne CP. RNA transcription modulates phase transition-driven nuclear body assembly. *Proc Natl Acad Sci*. 2015;112(38):E5237-E5245. doi:10.1073/pnas.1509317112
41. Liao S, Chen X, Xu T, et al. Antisense ribosomal siRNAs inhibit RNA polymerase I-directed transcription in C. elegans. *Nucleic Acids Res*. 2021;49(16):9194-9210. doi:10.1093/nar/gkab662
42. Korsholm LM, Gál Z, Nieto B, et al. Recent advances in the nucleolar responses to DNA double-strand breaks. *Nucleic Acids Res*. 2020;48(17):9449-9461. doi:10.1093/nar/gkaa713
43. Zhao Q, Rangan R, Weng S, Özdemir C, Cenik ES. Inhibition of ribosome biogenesis in the epidermis is sufficient to trigger organism-wide growth quiescence independently of nutritional status in C. elegans. *PLOS Biol*. 2023;21(8):e3002276. doi:10.1371/journal.pbio.3002276
44. Nousch M, Eckmann CR. Translational Control in the Caenorhabditis elegans Germ Line. In: Schedl T, ed. *Germ Cell Development in C. Elegans*. Springer; 2013:205-247. doi:10.1007/978-1-4614-4015-4_8
45. Racher H, Hansen D. Translational control in the C. elegans hermaphrodite germ line. *Genome*. 2010;53(2):83-102. doi:10.1139/G09-090
46. Pushpa K, Kumar GA, Subramaniam K. Translational Control of Germ Cell Decisions. *Results Probl Cell Differ*. 2017;59:175-200. doi:10.1007/978-3-319-44820-6_6
47. Iouk TL, Aitchison JD, Maguire S, Wozniak RW. Rrb1p, a Yeast Nuclear WD-Repeat Protein Involved in the Regulation of Ribosome Biosynthesis. *Mol Cell Biol*. 2001;21(4):1260-1271. doi:10.1128/MCB.21.4.1260-1271.2001
48. Bass HW, Marshall WF, Sedat JW, Agard DA, Cande WZ. Telomeres Cluster De Novo before the Initiation of Synapsis: A Three-dimensional Spatial Analysis of Telomere Positions before and during Meiotic Prophase. *J Cell Biol*. 1997;137(1):5-18. doi:10.1083/jcb.137.1.5
49. Chriss A, Börner GV, Ryan SD. Agent-based modeling of nuclear chromosome ensembles identifies determinants of homolog pairing during meiosis. *PLOS Comput Biol*. 2024;20(5):e1011416. doi:10.1371/journal.pcbi.1011416
50. MacQueen AJ, Villeneuve AM. Nuclear reorganization and homologous chromosome pairing during meiotic prophase require *C. elegans chk-2*. *Genes Dev*. 2001;15(13):1674-1687.

doi:10.1101/gad.902601

51. Ide S, Imai R, Ochi H, Maeshima K. Transcriptional suppression of ribosomal DNA with phase separation. *Sci Adv*. 2020;6(42):eabb5953. doi:10.1126/sciadv.abb5953
52. Reinke V, Gil IS, Ward S, Kazmer K. Genome-wide germline-enriched and sex-biased expression profiles in Caenorhabditis elegans. *Development*. 2004;131(2):311-323. doi:10.1242/dev.00914
53. Chiu TP, Xin B, Markarian N, Wang Y, Rohs R. TFBSshape: an expanded motif database for DNA shape features of transcription factor binding sites. *Nucleic Acids Res*. 2020;48(D1):D246-D255. doi:10.1093/nar/gkz970
54. Chi W, Reinke V. Promotion of oogenesis and embryogenesis in the C. elegans gonad by EFL-1/DPL-1 (E2F) does not require LIN-35 (pRB). *Development*. 2006;133(16):3147-3157. doi:10.1242/dev.02490
55. Angus-Hill ML, Schlichter A, Roberts D, Erdjument-Bromage H, Tempst P, Cairns BR. A Rsc3/Rsc30 Zinc Cluster Dimer Reveals Novel Roles for the Chromatin Remodeler RSC in Gene Expression and Cell Cycle Control. *Mol Cell*. 2001;7(4):741-751. doi:10.1016/S1097-2765(01)00219-2
56. Han M, Wei G, McManus CE, Hillier LW, Reinke V. Isolated C. elegans germ nuclei exhibit distinct genomic profiles of histone modification and gene expression. *BMC Genomics*. 2019;20:500. doi:10.1186/s12864-019-5893-9
57. McManus CE, Mazzetto M, Wei G, Han M, Reinke V. The zinc-finger protein OEF-1 stabilizes histone modification patterns and promotes efficient splicing in the Caenorhabditis elegans germline. *G3 GenesGenomesGenetics*. 2021;11(12):jkab329. doi:10.1093/g3journal/jkab329
58. Tabuchi TM, Rechtsteiner A, Jeffers TE, Egelhofer TA, Murphy CT, Strome S. Caenorhabditis elegans sperm carry a histone-based epigenetic memory of both spermatogenesis and oogenesis. *Nat Commun*. 2018;9(1):4310. doi:10.1038/s41467-018-06236-8
59. Li T, Kelly WG. A Role for Set1/MLL-Related Components in Epigenetic Regulation of the Caenorhabditis elegans Germ Line. Schübeler D, ed. *PLoS Genet*. 2011;7(3):e1001349. doi:10.1371/journal.pgen.1001349
60. Freeman TF, Zhao Q, Surya A, Rothe R, Cenik ES. Ribosome biogenesis disruption mediated chromatin structure changes revealed by SRAtac, a customizable end to end analysis pipeline for ATAC-seq. *BMC Genomics*. 2023;24(1):512. doi:10.1186/s12864-023-09576-y
61. Al-Refaie N, Padovani F, Hornung J, et al. Fasting shapes chromatin architecture through an mTOR/RNA Pol I axis. *Nat Cell Biol*. 2024;26(11):1903-1917. doi:10.1038/s41556-024-01512-w
62. Bersaglieri C, Kresoja-Rakic J, Gupta S, et al. Genome-wide maps of nucleolus interactions reveal distinct layers of repressive chromatin domains. *Nat Commun*. 2022;13(1):1483. doi:10.1038/s41467-022-29146-2
63. Hua L, Yan D, Wan C, Hu B. Nucleolus and Nucleolar Stress: From Cell Fate Decision to Disease Development. *Cells*. 2022;11(19):3017. doi:10.3390/cells11193017
64. Paredes S, Maggert KA. Ribosomal DNA contributes to global chromatin regulation. *Proc Natl Acad Sci*. 2009;106(42):17829-17834. doi:10.1073/pnas.0906811106
65. Wang C, Ma H, Baserga SJ, Pederson T, Huang S. Nucleolar structure connects with global nuclear organization. *Mol Biol Cell*. 2023;34(12):ar114. doi:10.1091/mbc.E23-02-0062
66. Potapova TA, Gerton JL. Ribosomal DNA and the nucleolus in the context of genome organization. *Chromosome Res*. 2019;27(1):109-127. doi:10.1007/s10577-018-9600-5

67. Bagijn MP, Goldstein LD, Sapetschnig A, et al. Function, Targets, and Evolution of Caenorhabditis elegans piRNAs. *Science*. 2012;337(6094):574-578. doi:10.1126/science.1220952
68. Gu W, Shirayama M, Conte D, et al. Distinct Argonaute-Mediated 22G-RNA Pathways Direct Genome Surveillance in the *C. elegans* Germline. *Mol Cell*. 2009;36(2):231-244. doi:10.1016/j.molcel.2009.09.020
69. Shen EZ, Chen H, Ozturk AR, et al. Identification of piRNA Binding Sites Reveals the Argonaute Regulatory Landscape of the *C. elegans* Germline. *Cell*. 2018;172(5):937-951.e18. doi:10.1016/j.cell.2018.02.002
70. Belew MD, Chien E, Wong M, Michael WM. The topoisomerase II/condensin II axis silences transcription during germline specification in *Caenorhabditis elegans*. Arbeitman M, ed. *G3 Genes Genomes Genet*. Published online October 3, 2024:jkae236. doi:10.1093/g3journal/jkae236
71. Crittenden SL, Bernstein DS, Bachorik JL, et al. A conserved RNA-binding protein controls germline stem cells in Caenorhabditis elegans. *Nature*. 2002;417(6889):660-663. doi:10.1038/nature754
72. Diag A, Schilling M, Klironomos F, Ayoub S, Rajewsky N. Spatiotemporal m(i)RNA Architecture and 3′ UTR Regulation in the *C. elegans* Germline. *Dev Cell*. 2018;47(6):785-800.e8. doi:10.1016/j.devcel.2018.10.005
73. Merritt C, Rasoloson D, Ko D, Seydoux G. 3′ UTRs Are the Primary Regulators of Gene Expression in the C. elegans Germline. *Curr Biol*. 2008;18(19):1476-1482. doi:10.1016/j.cub.2008.08.013
74. Wickens M, Bernstein DS, Kimble J, Parker R. A PUF family portrait: 3′UTR regulation as a way of life. *Trends Genet*. 2002;18(3):150-157. doi:10.1016/S0168-9525(01)02616-6
75. Deisenroth C, Franklin DA, Zhang Y. The Evolution of the Ribosomal Protein–MDM2–p53 Pathway. *Cold Spring Harb Perspect Med*. 2016;6(12):a026138. doi:10.1101/cshperspect.a026138
76. Hannan KM, Soo P, Wong MS, et al. Nuclear stabilization of p53 requires a functional nucleolar surveillance pathway. *Cell Rep*. 2022;41(5):111571. doi:10.1016/j.celrep.2022.111571
77. Ma H, Pederson T. The nucleolus stress response is coupled to an ATR-Chk1–mediated G2 arrest. *Mol Biol Cell*. 2013;24(9):1334-1342. doi:10.1091/mbc.e12-12-0881
78. Li W, Yanowitz JL. ATM and ATR Influence Meiotic Crossover Formation Through Antagonistic and Overlapping Functions in Caenorhabditis elegans. *Genetics*. 2019;212(2):431-443. doi:10.1534/genetics.119.302193
79. Yu Z, Kim HJ, Dernburg AF. ATM signaling modulates cohesin behavior in meiotic prophase and proliferating cells. *Nat Struct Mol Biol*. 2023;30(4):436-450. doi:10.1038/s41594-023-00929-5
80. Nottke AC, Beese-Sims SE, Pantalena LF, Reinke V, Shi Y, Colaiácovo MP. SPR-5 is a histone H3K4 demethylase with a role in meiotic double-strand break repair. *Proc Natl Acad Sci*. 2011;108(31):12805-12810. doi:10.1073/pnas.1102298108
81. Fulka H, Mrazek M, Fulka J. Nucleolar dysfunction may be associated with infertility in humans. *Fertil Steril*. 2004;82(2):486-487. doi:10.1016/j.fertnstert.2003.12.042
82. Sanchez E, Laplace-Builhé B, Mau-Them FT, et al. POLR1B and neural crest cell anomalies in Treacher Collins syndrome type 4. *Genet Med*. 2020;22(3):547-556. doi:10.1038/s41436-019-0669-9
83. Trainor PA. Craniofacial birth defects: The role of neural crest cells in the etiology and pathogenesis of Treacher Collins syndrome and the potential for prevention. *Am J Med Genet A*.

2010;152A(12):2984-2994. doi:10.1002/ajmg.a.33454

84. Dickinson DJ, Pani AM, Heppert JK, Higgins CD, Goldstein B. Streamlined Genome Engineering with a Self-Excising Drug Selection Cassette. *Genetics*. 2015;200(4):1035-1049. doi:10.1534/genetics.115.178335
85. Stirling DR, Swain-Bowden MJ, Lucas AM, Carpenter AE, Cimini BA, Goodman A. CellProfiler 4: improvements in speed, utility and usability. *BMC Bioinformatics*. 2021;22(1):433. doi:10.1186/s12859-021-04344-9
86. R: A Language and Environment for Statistical Computing. Published online 2023. https://www.R-project.org/
87. Bankhead P, Loughrey MB, Fernández JA, et al. QuPath: Open source software for digital pathology image analysis. *Sci Rep*. 2017;7(1):16878. doi:10.1038/s41598-017-17204-5
88. Schneider CA, Rasband WS, Eliceiri KW. NIH Image to ImageJ: 25 years of image analysis. *Nat Methods*. 2012;9(7):671-675. doi:10.1038/nmeth.2089
89. Martin M. Cutadapt removes adapter sequences from high-throughput sequencing reads. *EMBnet.journal*. 2011;17(1):10-12. doi:10.14806/ej.17.1.200
90. Kim D, Paggi JM, Park C, Bennett C, Salzberg SL. Graph-based genome alignment and genotyping with HISAT2 and HISAT-genotype. *Nat Biotechnol*. 2019;37(8):907-915. doi:10.1038/s41587-019-0201-4
91. Picard toolkit. Published online 2019. Accessed December 12, 2023. https://broadinstitute.github.io/picard/
92. Liao Y, Smyth GK, Shi W. featureCounts: an efficient general purpose program for assigning sequence reads to genomic features. *Bioinformatics*. 2014;30(7):923-930. doi:10.1093/bioinformatics/btt656
93. Ramírez F, Ryan DP, Grüning B, et al. deepTools2: a next generation web server for deep-sequencing data analysis. *Nucleic Acids Res*. 2016;44(W1):W160-W165. doi:10.1093/nar/gkw257
94. Hahne F, Durinck S, Ivanek R, et al. Gviz: Plotting data and annotation information along genomic coordinates. Published online 2023. doi:10.18129/B9.bioc.Gviz
95. Love MI, Huber W, Anders S. Moderated estimation of fold change and dispersion for RNA-seq data with DESeq2. *Genome Biol*. 2014;15(12):550. doi:10.1186/s13059-014-0550-8
96. Risso D, Ngai J, Speed TP, Dudoit S. Normalization of RNA-seq data using factor analysis of control genes or samples. *Nat Biotechnol*. 2014;32(9):896-902. doi:10.1038/nbt.2931
97. Chen Y, Lun ATL, Smyth GK. From reads to genes to pathways: differential expression analysis of RNA-Seq experiments using Rsubread and the edgeR quasi-likelihood pipeline. Published online August 2, 2016. doi:10.12688/f1000research.8987.2
98. Zhu A, Ibrahim JG, Love MI. Heavy-tailed prior distributions for sequence count data: removing the noise and preserving large differences. *Bioinformatics*. 2019;35(12):2084-2092. doi:10.1093/bioinformatics/bty895
99. Wang Q, Li M, Wu T, et al. Exploring Epigenomic Datasets by ChIPseeker. *Curr Protoc*. 2022;2(10):e585. doi:10.1002/cpz1.585
100. Annotation package for TxDb object(s). Published online 2019. Accessed December 12, 2023. http://bioconductor.org/packages/TxDb.Celegans.UCSC.ce11.refGene/
101. Wu T, Hu E, Xu S, et al. clusterProfiler 4.0: A universal enrichment tool for interpreting omics data. *The Innovation*. 2021;2(3):100141. doi:10.1016/j.xinn.2021.100141

102. Yu G, Wang LG, Han Y, He QY. clusterProfiler: an R Package for Comparing Biological Themes Among Gene Clusters. *OMICS J Integr Biol*. 2012;16(5):284-287. doi:10.1089/omi.2011.0118
103. Yu G, Gao CH. enrichplot: Visualization of Functional Enrichment Result. Published online 2024. https://yulab-smu.top/biomedical-knowledge-mining-book/
104. Bailey TL, Johnson J, Grant CE, Noble WS. The MEME Suite. *Nucleic Acids Res*. 2015;43(W1):W39-W49. doi:10.1093/nar/gkv416
105. Bailey TL. STREME: accurate and versatile sequence motif discovery. *Bioinformatics*. 2021;37(18):2834-2840. doi:10.1093/bioinformatics/btab203
106. Gupta S, Stamatoyannopoulos JA, Bailey TL, Noble WS. Quantifying similarity between motifs. *Genome Biol*. 2007;8(2):R24. doi:10.1186/gb-2007-8-2-r24
107. Lawrence M, Huber W, Pagès H, et al. Software for Computing and Annotating Genomic Ranges. *PLOS Comput Biol*. 2013;9(8):e1003118. doi:10.1371/journal.pcbi.1003118
108. SRA Toolkit Development Team. SRA Toolkit. https://trace.ncbi.nlm.nih.gov/Traces/sra/sra.cgi?view=software
109. Ewels PA, Peltzer A, Fillinger S, et al. The nf-core framework for community-curated bioinformatics pipelines. *Nat Biotechnol*. 2020;38(3):276-278. doi:10.1038/s41587-020-0439-x
110. nf-core/chipseq. https://doi.org/10.5281/zenodo.3240506
111. Kent J, UCSC Genome Browser Group. faCount. https://hgdownload.soe.ucsc.edu/admin/exe/linux.x86_64/faCount
112. Schmidt U, Weigert M, Broaddus C, Myers G. Cell Detection with Star-Convex Polygons. In: Frangi AF, Schnabel JA, Davatzikos C, Alberola-López C, Fichtinger G, eds. *Medical Image Computing and Computer Assisted Intervention – MICCAI 2018*. Springer International Publishing; 2018:265-273. doi:10.1007/978-3-030-00934-2_30
113. Toraason E, Adler VL, Kurhanewicz NA, et al. Automated and customizable quantitative image analysis of whole Caenorhabditis elegans germlines. *Genetics*. 2021;217(3):iyab010. doi:10.1093/genetics/iyab010